Cross Validation of Active and Passive Microwave Snowfall Products over the Continental United States

KAMIL MROZ,[a] MARIO MONTOPOLI,[b] ALESSANDRO BATTAGLIA,[c,d] GIULIA PANEGROSSI,[b] PIERRE KIRSTETTER,[e,f,g,h] AND LUCA BALDINI[b]

[a] *National Centre for Earth Observation, University of Leicester, Leicester, United Kingdom*
[b] *Institute of Atmospheric Sciences and Climate, National Research Council of Italy, Rome, Italy*
[c] *Department of Environmental, Land and Infrastructure Engineering (DIATI), Politecnico di Torino, Torino, Italy*
[d] *Earth Observation Science, Department of Physics and Astronomy, University of Leicester, Leicester, United Kingdom*
[e] *School of Meteorology, University of Oklahoma, Norman, Oklahoma*
[f] *School of Civil Engineering and Environmental Sciences, University of Oklahoma, Norman, Oklahoma*
[g] *NOAA/National Severe Storms Laboratory, Norman, Oklahoma*
[h] *Advanced Radar Research Center, University of Oklahoma, Norman, Oklahoma*

(Manuscript received 14 September 2020, in final form 1 March 2021)

ABSTRACT: Surface snowfall rate estimates from the Global Precipitation Measurement (GPM) mission's *Core Observatory* sensors and the *CloudSat* radar are compared to those from the Multi-Radar Multi-Sensor (MRMS) radar composite product over the continental United States during the period from November 2014 to September 2020. The analysis includes the Dual-Frequency Precipitation Radar (DPR) retrieval and its single-frequency counterparts, the GPM Combined Radar Radiometer Algorithm (CORRA), the *CloudSat* Snow Profile product (2C-SNOW-PROFILE), and two passive microwave retrievals, i.e., the Goddard Profiling algorithm (GPROF) and the Snow Retrieval Algorithm for GMI (SLALOM). The 2C-SNOW retrieval has the highest Heidke skill score (HSS) for detecting snowfall among the products analyzed. SLALOM ranks second; it outperforms GPROF and the other GPM algorithms, all detecting only 30% of the snow events. Since SLALOM is trained with 2C-SNOW, it suggests that the optimal use of the information content in the GMI observations critically depends on the precipitation training dataset. All the retrievals underestimate snowfall rates by a factor of 2 compared to MRMS. Large discrepancies (RMSE of 0.7–1.5 mm h^{-1}) between spaceborne and ground-based snowfall rate estimates are attributed to the complexity of the ice scattering properties and to the limitations of the remote sensing systems: the DPR instrument has low sensitivity, while the radiometric measurements are affected by the confounding effects of the background surface emissivity and of the emission of supercooled liquid droplet layers.

KEYWORDS: Snow; Snowfall; Hydrometeorology; Snow cover; Remote sensing; Satellite observations

1. Introduction

The Global Energy and Water Exchanges project (GEWEX) initiative of the World Climate Research Program continues to struggle with a lack of accurate precipitation estimates at high latitudes where precipitation occurs mainly as snowfall (Joe et al. 2010; Stephens et al. 2018; Liu 2020). The IPCC (2013) reported an additional surplus of 4 W m^{-2} of radiative flux into the surface compared to the previous energy budget, which has been compensated by an increase of the latent heat flux and attributed to snowfall at high latitudes (Stephens et al. 2012; L'Ecuyer et al. 2015). This epitomizes that accurate snowfall estimates are key to establish a baseline against which changes in Earth's water and energy budgets can be measured. Little is also known about the impact of climate change on solid precipitation, though indications suggest that high-latitude precipitation has been increasing since the beginning of the century (Surussavadee and Staelin 2009) and its intensification is predicted by climate models (Lau et al. 2013). Quantifying snowfall rates is crucial for estimating snow water accumulation at the surface (Lettenmaier et al. 2015), which is essential for advancing our understanding of polar processes. Finally, snowfall and its eventual melt and runoff affects water resources (Skofronick-Jackson et al. 2019) and feedbacks on the thermohaline circulation.

High-latitude in situ measurements of precipitation are still rare due to the remoteness of these regions, and are fraught with problems like undercatch and wind-blown snow biases (Fassnacht 2004). This measurement gap can be bridged by spaceborne active and passive microwave (PMW) sensors that are tailored to detect and quantify snowfall thanks to their ability to probe within clouds (Levizzani et al. 2011; Skofronick-Jackson et al. 2017).

Two spaceborne radars paved the way toward groundbreaking vertically resolved observations of falling snow over

Denotes content that is immediately available upon publication as open access.

Corresponding author: Kamil Mroz, kamil.mroz@le.ac.uk

DOI: 10.1175/JHM-D-20-0222.1

much of the globe: the *CloudSat* Cloud Profiling Radar (CPR; Tanelli et al. 2008) and the Global Precipitation Measurement (GPM) mission Dual-Frequency Precipitation Radar (DPR; Skofronick-Jackson et al. 2017). The CPR was developed by the National Aeronautics and Space Administration (NASA), while the DPR was built by the Japan Aerospace Exploration Agency (JAXA). Both sensors have provided novel snowfall climatologies (e.g., Wood and L'Ecuyer 2018; Kulie et al. 2016; Milani et al. 2018; Palerme et al. 2014; Bennartz et al. 2019; Kulie et al. 2020) which have been thoroughly discussed and intercompared in Skofronick-Jackson et al. (2019).

PMW sensors are promising for snowfall characterization as well, with high-frequency channels (90–190 GHz) generally sensitive to ice scattering (Bennartz and Bauer 2003; Skofronick-Jackson and Johnson 2011; Liu and Seo 2013). Since PMW radiometers have a large swath and are installed on multiple platforms, they ensure good global coverage and long data records. Physical and empirical approaches have been developed for snowfall retrievals using PMW radiometers, including conically scanning radiometers such as the Special Sensor Microwave water vapor sounder (SSM/T2; Liu and Curry 1997), the Special Sensor Microwave Imager/Sounder (SSMIS; You et al. 2015), and the Global Precipitation Measurement Microwave Imager (GMI; Rysman et al. 2018; Takbiri et al. 2019); and cross-track-scanning radiometers like the Advanced Microwave Sounding Unit-B (AMSU-B) and Microwave Humidity Sounder (MHS; Kongoli et al. 2003; Ferraro et al. 2005; Surussavadee and Staelin 2009; Noh et al. 2009; Liu and Seo 2013) and the Advanced Technology Microwave Sounder (ATMS; Kongoli et al. 2015; Meng et al. 2020). The launch of the GPM *Core Observatory* fostered the development of combined radar–radiometer snowfall algorithms, such as the Combined Radar Radiometer Algorithm (CORRA; Grecu et al. 2016; Grecu and Olson 2020).

Both active and passive microwave-based snowfall remote sensing remains challenging because snowfall scattering properties (backscattering and extinction in particular), that are germane for converting measurements into physical quantities like snow rates and ice contents, depend on complicated shape of snowflakes (e.g., Petty and Huang 2010; Kuo et al. 2016; Liu 2020; Kneifel et al. 2020). Since snow precipitating systems are often composed of a vast gamut of snow habit types with a variety of densities, shapes and sizes, microphysical retrievals are generally characterized by large uncertainties. For spaceborne radars, additional limitations come from the contamination by the ground clutter in the lowest 1000 m (Bennartz et al. 2019; Palerme et al. 2019), the limited coverage, the low sensitivity for the DPR (Casella et al. 2017; Skofronick-Jackson et al. 2019), and the reflectivity saturation at high snow rates for the CPR (Cao et al. 2014; Liu 2020). For PMW sensors, two extra issues are encountered. First, the weak snowfall scattering signal can be masked by the increased atmospheric emission from supercooled cloud droplets (Kneifel et al. 2010; Liu and Seo 2013; Wang et al. 2013; Panegrossi et al. 2017). Second, the changes in the surface emissivity due to snow accumulation (and its subsequent metamorphosis) and/or sea ice variability can be confused with the snow hydrometeor microwave signal (Noh et al. 2009; Turk et al. 2014; Munchak et al. 2020; Takbiri et al. 2019). These issues highlight the need to properly characterize the microwave surface properties at the time of the overpass, especially at high latitudes and in cold and dry conditions, when the high-frequency channels are more affected (Panegrossi et al. 2017; You et al. 2016; Ebtehaj and Kummerow 2017; Munchak et al. 2020).

Satellite microwave snowfall products have previously been validated with ground-based radar algorithms (Cao et al. 2014; Norin et al. 2015; Matrosov 2019; von Lerber et al. 2018; Smalley et al. 2017; Meng et al. 2020). In such studies, both the detection skill and the quantitative estimation of surface snowfall rates are typically assessed. However, such validation efforts are usually restricted to a single satellite snowfall product (e.g., Bennartz et al. 2019). In this paper, we capitalize on the availability over the past few winter seasons of both the CPR and GPM data, and of the Multi-Radar Multi-Sensor (MRMS; Zhang et al. 2016) system version 11 snowfall rates over the continental United States (CONUS). This allows for an extensive intercomparison of the MRMS precipitation data with the radar-only (both CPR and DPR), radiometer-only (GMI), and combined (GMI and DPR) snowfall retrievals.

Section 2a presents a description of the ground-based MRMS product which is used as a benchmark for a number of spaceborne retrievals described in section 2b. The methodology of the comparison is presented in section 3, while the main results can be found in section 4. Conclusions are drawn and the study is summarized in section 5.

2. Snow precipitation products

This section briefly describes the characteristics of the ground reference data and the different satellite snowfall products used for the intercomparison.

a. The ground reference Multi-Radar Multi-Sensor dataset

The U.S. Next Generation Weather Radar (NEXRAD) network of 160 S-band Weather Surveillance Radar-1988 Doppler (WSR-88D) radars, operated by the National Weather Service (NWS), together with 30 Canadian radars, mostly operated by the Meteorological Service of Canada (MSC), provide the main input to the MRMS dataset. The coverage of the MRMS domain, along with the location of all the radars that are feeding the MRMS products, is shown in Fig. 1.

Rapid (3–10 min) radar volume scans, numerical model outputs (i.e., freezing-level height, temperature, wind, and relative humidity) from the Rapid Update Cycle (RAP) and automated gauge networks, such as the Hydrometeorological Automated Data System (HADS; Kim et al. 2009) and the Meteorological Assimilation Data Ingest System (MADIS; Miller et al. 2007), feed algorithms that generate hydrometeorological products at the resolution of 0.01° × 0.01° every 2 min (Zhang et al. 2016). The MRMS system generates seamless real-time and high-resolution precipitation products over the CONUS (130°–60°W; 22°–55°N), including snowfall. These products support many meteorological, hydrological and aviation applications. Moreover, NEXRAD's polarimetric

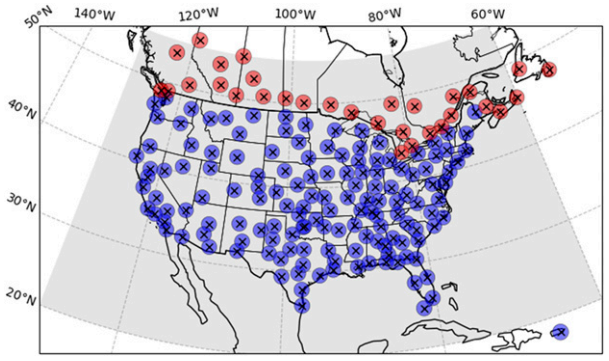

FIG. 1. A map of the study area. Gray shading indicates the spatial extent of the MRMS products, crosses show the location of the radars, while circles indicate 100-km range. Red and blue colors correspond to the U.S. and Canadian instruments, respectively.

capabilities allow for the removal of nonhydrometeor echoes, which makes MRMS a very reliable precipitation detector. An example of two products (precipitation rate and precipitation type) showing a snapshot of the March 2017 North American blizzard is presented in Fig. 2.

Because most of the gauges that are feeding into the MRMS system are tipping buckets, which encounter issues in measuring snowfall accurately (Martinaitis et al. 2015; Rasmussen et al. 2012; Wen et al. 2017), instantaneous precipitation rate values based on the radar-only measurements are used in this study. In this product, the near-surface snow precipitation rate, PR_{MRMS}, is obtained from the reflectivity-to-snow relationship $Z = 75PR_{MRMS}^2$ (Zhang et al. 2016; Kirstetter et al. 2015, 2018), which is equivalent to

$$PR_{MRMS}(Z) = 0.12Z^{0.5}. \quad (1)$$

To identify snowfall, two criteria are used. First, the S-band radar reflectivity factor Z must exceed 5 dBZ in order to avoid echoes caused by Bragg scattering (Kollias et al. 2007). Second, surface and wet-bulb temperatures derived from hourly model analyses must be lower than 2° and 0°C, respectively. The threshold value imposed on the reflectivity limits the MRMS sensitivity to snowfall rates higher than 0.2 mm h^{-1}.

The validation of the GPM snowfall algorithms is performed over the period spanning between November 2014 and September 2020. The ground-based data for the analysis were obtained from Iowa State University (they are freely available at https://mtarchive.geol.iastate.edu/). The *CloudSat* product is validated with the same dataset close to the end of the mission, i.e., until November 2017, but additionally the single-polarization MRMS data of Zhang and Gourley (2018) covering the period between 2006 and 2011 are used. Note that the old product is characterized by a lower time resolution (5 min) and it lacks the polarimetric quality control, which may affect the accuracy of the collocation. Despite these limitations, the inclusion of these data greatly increases the validation dataset size (*CloudSat* CPR was fully operational during 2006–11

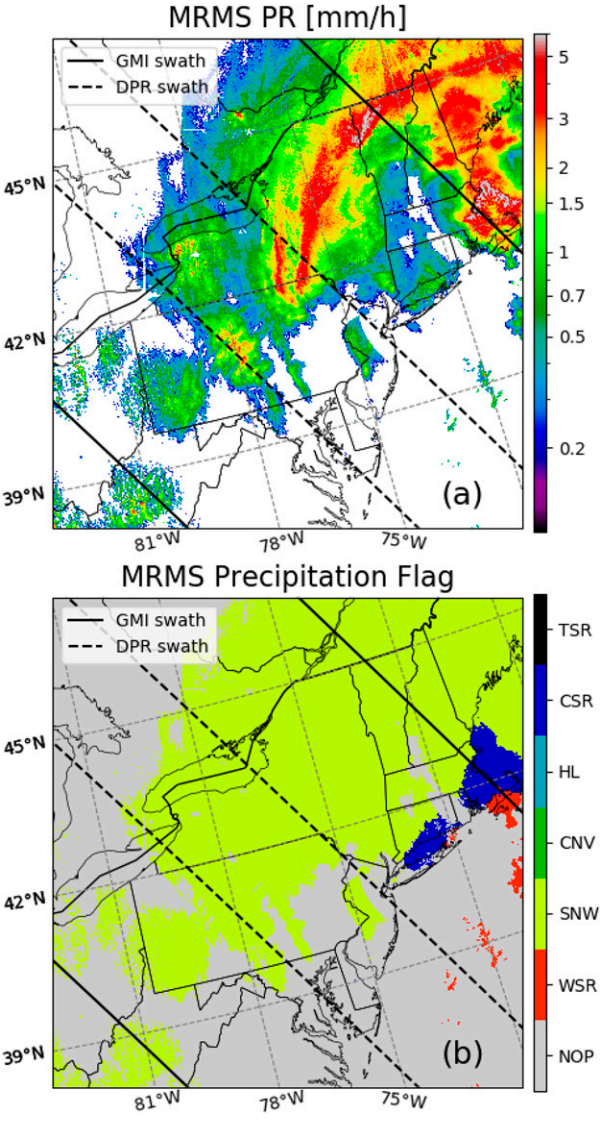

FIG. 2. An example of MRMS products over the northeast United States at 2002 UTC 14 Mar 2017. (a) Instantaneous precipitation rate (PR) derived every 2 min from the radar measurements. (b) Precipitation phase flag (NOP—no precipitation; WSR—warm stratiform rain; SNW—snow; CNV—convection; HL—hail; CSR—cold stratiform rain; TSR—tropical stratiform rain).

whereas it has been operated in daylight only after a battery anomaly in March 2011).

b. Satellite products

The description of the satellite precipitation products is divided into subsections that reflect the instrument used for the retrieval.

1) GPM-DPR PRODUCTS (DPR, KU AND KA ONLY)

The GPM-DPR products provide precipitation estimates as single-frequency (SF) algorithms, based on measurement collected only at Ku band or only at Ka band, as well as

dual-frequency (DF) retrievals that take advantage of the dual-frequency measurements for the collocated Ku- and Ka-band pixels. In this study, we use the DPR, Ku and Ka version 06 products (Iguchi and Meneghini 2017, 2016b,a). These algorithms follow the same modular procedure, with some differences in the design for the DF and SF products. First, the clutter-free ranges closest to the ground are identified and it is determined whether precipitation reaches the surface. Second, the surface reference technique (SRT) is used to estimate the path-integrated attenuation (PIA) for each frequency due to the propagation through precipitation using the radar returns from the surface (Meneghini et al. 2000). Different variations of the technique are run and a combination of them provides the final PIA-SRT estimate (Liao and Meneghini 2019). From version 06, an additional PIA estimate based on the power-law relation between the reflectivity and the attenuation (see Hitschfeld and Bordan 1954) is calculated. This new PIA estimate was shown to reduce erroneously large precipitation estimates near coasts and it leads to a better agreement with the validation data over the United States. The attenuation due to nonprecipitating cloud and atmospheric gases is calculated from the ancillary environmental data provided by the Japan Meteorological Agency Global Analysis (GANAL) model. Next, the classification module labels precipitation types and provides information on the melting layer through distinct SF and DF algorithms. The probability of snow at the surface, based on the slope of the dual-frequency wavelength ratio (DWR), the storm-top height, and the maximum of the measured Ku-band reflectivity, is provided (Le and Chandrasekar 2019) by the DF product only. The drop size distribution (DSD) module sets the physical properties relative to the precipitation phase that are used for simulating the radar reflectivities. The DSD is assumed to follow a normalized gamma function. Assuming a shape parameter fixed to 3, only two parameters are retrieved, namely, the intercept N_w of the normalized distribution and the mass-weighted mean diameter D_m. These parameters are obtained by iteratively fitting the measurements by imposing a relationship between D_m and the precipitation rate (Seto and Kinoshita 2015; Seto and Shimozuma 2015). An adjustment factor ε, conceived to solve inconsistencies between attenuation estimates obtained by the different attenuation estimation techniques (Seto and Iguchi 2015), is computed for each precipitation column.

2) *CloudSat* CPR product: 2C-SNOW-PROFILE

The *CloudSat* Snow Profile product (2C-SNOW-PROFILE; Wood and L'Ecuyer 2018) estimates vertical profiles of snow properties, such as snowfall rate, snow size distribution parameters and snow water content, from the measured profiles of *CloudSat* CPR reflectivity. The estimated snow properties are obtained using an optimal estimation retrieval approach (Rodgers 2000), which is applied where the 2C-PRECIP CPR product indicates surface snow probable or certain or if the estimated liquid fraction is less than 10%–15% (dry snow). The 2C-SNOW-PROFILE algorithm follows four steps. First, the clutter-contaminated range bins near the surface are detected and excluded (the clutter region ranges from 500 m for ocean without sea ice or inland water to 1000 m for all other surfaces). Second, the snow layers are identified looking at contiguous radar bins located at temperatures below 0°C, as inferred from the ECMWF-AUX temperature profiles. Third, an optimal estimation method is adopted to retrieve the two free parameters (i.e., slope and intercept) of the assumed exponential snow size distribution (Marshall and Palmer 1948); fourth, the snowfall rate is calculated for the estimated particle size distribution based on explicit, physically based, mass–size and velocity–size relations specific to snow (Mitchell 1996).

3) GMI-GPROF

The Goddard Profiling algorithm (GPROF; Kummerow et al. 2015) is the NASA operational precipitation retrieval algorithm for the GPM passive microwave radiometers constellation, including the GPM Microwave Imager (GMI). For each set of multifrequency GMI brightness temperatures, GPROF provides a cloud and precipitation profile derived from a predefined database of possible solutions (referred to as an a priori database) based on a Bayesian inversion scheme. To limit the solution search only to appropriate cloud regimes, the a priori database is partitioned using various ancillary data: the 2-m temperature (T2m) and the total precipitable water (TPW) from reanalyses and the surface type classification. The surface types are obtained from a SSM/I-observed emissivity climatology (Aires et al. 2011) and its daily updates by NOAA's AutoSnow product (Romanov et al. 2000). The GMI GPROF version 05 product (Iguchi and Meneghini 2016c) tested in this study, considers different sources of precipitation retrievals to build its a priori database depending on the surface type detected in the GMI IFOV. The Ku-band and the DPR combined version 04 algorithms (Ku-V04, CORRA-V04) are used to build the database over "land" (i.e., vegetated surfaces, inland waters, and coastlines) and "ocean" (i.e., oceans, sea ice, and sea ice/ocean boundaries), respectively (see Grecu et al. 2004, 2016). Alternatively, MRMS is used over snow-covered-land surfaces. One year of Ku-V04, CORRA-V04 retrievals (from September 2014 to August 2015) and two years of matched MRMS data (from April 2014 to August 2016) populate the a priori dataset. Out of the three different precipitation estimates provided by GPROF (surfacePrecipitation, mostLikelyPrecipitation, frozenPrecipitation), only the surfacePrecipitation product is assessed for the agreement with MRMS in this study. The frozenPrecipitation product, or more specifically its ratio to the surfacePrecipitation retrieval, is only used as a measure of the snow probability according to GPROF. The quantitative evaluation against MRMS is performed where the ratio exceeds 0.9 which ensures that GPROF is predominantly retrieving snow.

4) GMI-SLALOM

The Snow Retrieval Algorithm for GMI (SLALOM; Rysman et al. 2018, 2019), developed at CNR-ISAC under the EUMETSAT Satellite Application Facility for Operational Hydrology and Water Management (H SAF) program, is a frozen-precipitation-only retrieval algorithm based on machine learning, primarily designed for the GMI. SLALOM

inputs all 13 GMI channels together with ancillary variables describing the atmospheric conditions (e.g., ERA-Interim T2m, TPW, humidity profiles). In contrast to the GPROF algorithm, SLALOM does not consider any background information on the surface type. SLALOM is composed of four modules: (i) the snowfall detection, (ii) the supercooled droplet at cloud-top detection, (iii) the snow water path (SWP), and (iv) the surface snowfall rate (SSR) estimation modules. The snowfall and supercooled detection modules rely mainly on the random forest approach, while the SWP and SSR retrieval modules use a segmented multilinear regression approach and a gradient boosting method, respectively. SLALOM SWP and SSR retrievals are trained on the CPR 2C-SNOW-PROFILE product using a GMI/*CloudSat* coincidence dataset (2B-CSATGPM product V03B; Turk 2016) that is mostly populated at higher latitudes, largely around 60°N/S. The snowfall and supercooled droplet detection is trained using the *CloudSat* and *CALIPSO* radar–lidar (DARDAR; Delanoë and Hogan 2008) cloud classification product.

5) CORRA

The GPM Combined Radar Radiometer Algorithm (CORRA; Grecu et al. 2016) integrates the DPR and the GMI into a physically consistent precipitation product. CORRA is based on the optimal estimation method. A physical forward model based on the soft-sphere approximation is used to build lookup tables and simulate satellite radar and radiometer observations as a function of the state vector, at all frequencies of interest. The forward operator accounts for nonuniform beam filling (Durden et al. 1998; Zhang et al. 2004) and multiple scattering effects (Hogan and Battaglia 2008). The observation vector includes the profile of Ka-band radar reflectivity, the GMI brightness temperatures downscaled to the DPR footprint (using the methodology of Bauer and Bennartz 1998) and the radar path-integrated attenuation estimates. The unknown vector has a single unknown for each radar bin, i.e., the intercept parameter of the normalized gamma particle size distribution (Testud et al. 2001). The shape parameter of the distribution μ is left fixed while the weighted mean diameter D_m is diagnosed using Ku-band reflectivity data alone based on a first guess assumption on the N_w profile (Iguchi et al. 2000). As it is done for the DPR products, determination of the precipitation phase at the ground is based on the brightband detection in the clutter-free bins. This study uses version 06 of the CORRA product (Olson 2017).

3. Methodology

Comparisons between spaceborne and ground-based products require spatial and temporal collocation. In this study, the temporal collocation is addressed by selecting the MRMS algorithm output that is closest in time to the satellite overpass. To perform spatial matching, the MRMS product is coarsened to the horizontal resolution of the DPR and the 36-GHz channel of the GMI ($5 \times 5\,\text{km}^2$ and $15 \times 9\,\text{km}^2$, respectively). Although the horizontal resolution of the MRMS grid is only slightly better than that of the *CloudSat* retrieval ($1.4 \times 1.7\,\text{km}^2$), it is also coarsened prior to the comparison with the 2C-SNOW product. The spatial coarsening is performed for each overpass by weighting and then averaging the MRMS precipitation rates within the spaceborne instrument field of view (IFOV) with a Gaussian approximation of the two-way antenna gain (details in Mroz et al. 2017). An example of the MRMS precipitation output matched with the GMI resolution is presented in Fig. 3 along with the GPROF and DPR products.

The MRMS precipitation type product is used to calculate the fraction of the spaceborne sensor footprint that is occupied by solid and liquid precipitation phases (see Fig. 3a). The precipitation phase from GPROF and the DPR is presented in Figs. 3b and 3c for comparison. Since GPROF does not provide a categorical precipitation phase (solid/liquid/melting), the frozen fraction is obtained as a ratio between the GPROF frozen precipitation product (frozenPrecipitation) and the GPROF total precipitation rate (surfacePrecipitation). There is a clear correspondence between the precipitation phase reported by the MRMS and GPROF products and the contour of the 0°C isotherm of the 2-m wet-bulb temperature that is derived from ECMWF ERA5 reanalysis data. This indicates that both of them rely on the ambient temperature information provided by ancillary data and differences in the probability of solid precipitation might result from using different numerical analysis input fields. The phase classification of the DPR is not in agreement with MRMS and GPROF over Lake Michigan. On one hand, the ranging capability of the spaceborne radar allows the detection of a bright band associated to the melting layer, which ensures high confidence in the rain detection. On the other hand, signatures of melting can be masked by surface clutter that can lead to too-frequent classification of snowfall precipitation (Watters et al. 2018; Skofronick-Jackson et al. 2019). Thus, it remains questionable which algorithm is closer to the truth for this case study. Because the determination of the precipitation phase is not the focus of this work, the detection capabilities of different products are evaluated independently of their corresponding phase flags. The environmental data from ECMWF ERA5 reanalysis (wet-bulb temperature, skin temperature, and near-surface ambient temperature gradient) are fed into the model of Sims and Liu (2015) to determine if the environmental conditions at the ground are favorable for snowfall. The assessment of the detection capabilities of the products is performed over pixels where the probability of frozen precipitation exceeds 90% according to the ECMWF data, regardless of the precipitation phase classifiers of each algorithm. Moreover, to minimize nonuniform beam filling issues, only those spaceborne footprints that are either completely empty or at least half-filled with nonzero PRs are considered. In case of the *CloudSat* product, all the MRMS native resolution pixels within 2 km from the satellite footprint center must be filled to be included in the intercomparison dataset. When adopting these thresholds, we account for approximately 95% of the precipitation volume reported by the ground-based product. By including the empty pixels in the dataset, the number of false snow warnings can be rigorously quantified.

Note that comparing precipitation intensity when the validation and the spaceborne datasets disagree on the precipitation

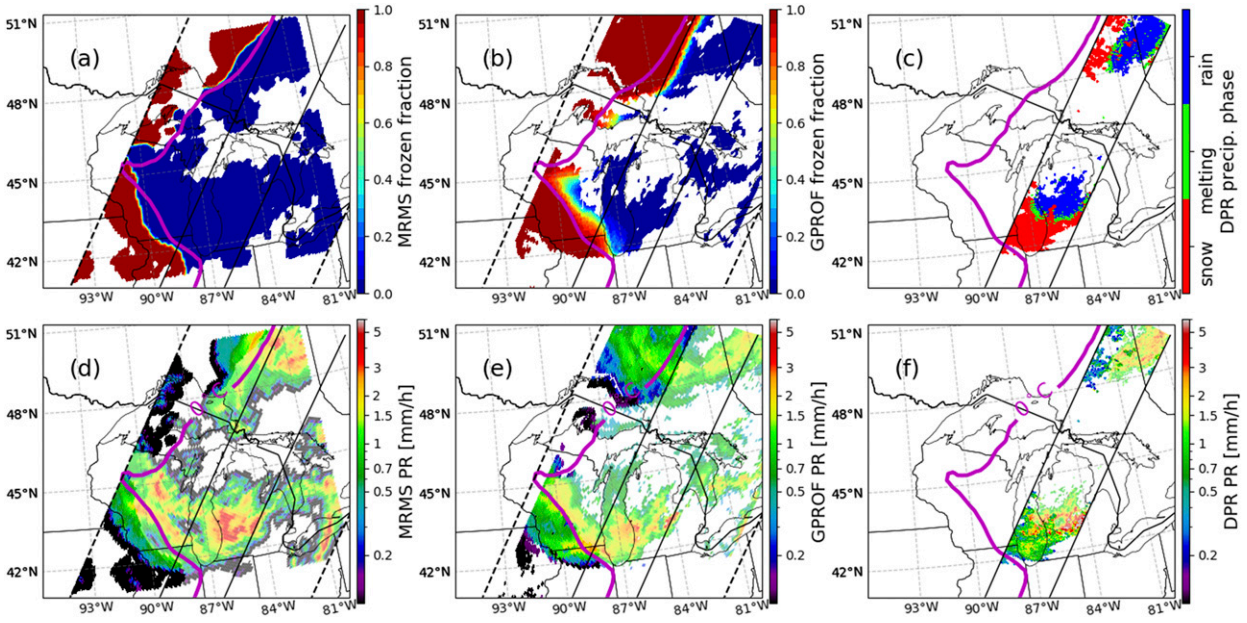

FIG. 3. The 18 Nov 2014 case study. (a)–(c) Precipitation phase at the ground as derived by MRMS, GPROF, and DPR products at 1756 UTC, respectively. (d)–(f) The corresponding surface precipitation rates from different algorithms. The faint colors indicate regions where rain or melting snow is present at the ground. The dashed (solid) lines mark the edges of the GMI (DPR) swath. The thick magenta line marks the 0°C isotherm of the wet-bulb temperature at 2-m height according to the ERA5 ECMWF reanalysis data.

phase may bias the quantitative comparison (mean error, RMSE, and other statistics). This issue does not affect SLALOM and 2C-SNOW products as they report precipitation intensity subject to being in a solid form. To avoid any potential biases, the quantitative validation presented in section 4c is performed only where both the MRMS and the satellite algorithms indicate solid phase precipitation. To determine the precipitation phase in the DPR products we use phaseNearSurface flag, for CORRA surfLiqRateFrac is used, while the ratio of frozenPrecipitation to surfacePrecipitation is utilized for GPROF. For MRMS, only the coarsened pixels where no rain contamination is present (i.e., all MRMS 1-km pixels within the spaceborne footprint are flagged as snow) are considered.

Prior to the analysis, the MRMS validation dataset is quality controlled. The data points that correspond to precipitation rates exceeding 21.3 mm h^{-1} are removed. Such snowfall corresponds to a radar reflectivity of 45 dBZ that is commonly used as a threshold for hail detection (Mroz et al. 2017) or a signature of ground clutter contamination. Another issue that affects the remote ground-based detection is the decreasing vertical resolution with range. It results in a reduced sensitivity and an increasing blind zone height above the surface while moving away from the radar. For instance, at a range of 50, 100, and 150 km any targets below 150, 600, 1300 m, respectively, are invisible to the radar. If the system has a beamwidth of 1°, its vertical resolution is reduced from approximately 900 m at 50 km to 2600 m at 150 km, over which span the sensitivity drops by 9.5 dB. This problem can strongly affect the assessment of the snowfall detection capabilities from space, since any precipitation in the blind zone of the ground-based radar would be interpreted as a false alarm for the satellite product. To quantify this effect, the validation data were split into nine range-dependent groups. Each group corresponds to an equal-area ring with the inner (outer) radius ranging from 0 to 141.4 km (50–150 km). Figure 4a shows the false alarm ratio (FAR) for each spaceborne retrieval as a function of the ring radius. For this analysis, very weak snowfall rates (below approximately 0.1 mm h^{-1} that are undetectable by MRMS but reported by spaceborne algorithms are treated as a correct rejection in the satellite product (see the discussion below and Table 1). Although the detection capabilities of the spaceborne sensors should not depend on the distance from the ground-based instruments, the FAR clearly increases as the range gets larger, with SLALOM and 2C-SNOW being the most affected. An initial drop in the number of the false alarms observed for the 2C-SNOW, CORRA, DPR, and Ku-only algorithms may correspond to the ground clutter effect in the spaceborne measurements. In other words, at very close ranges where ground-based radar samples close to the ground, the signal of the spaceborne systems can be contaminated by the surface return which results in some false alarms from space. As the range increases, the blind zone of two sensors becomes comparable and thus the FAR decreases. When the distance from the ground-based radar exceeds approximately 110 km, the FAR of the satellite products is rapidly increasing because they correctly report precipitation that occurs in the blind zone of the MRMS radars. This indicates that the evaluation of the detection capabilities of the spaceborne sensors should be performed in proximity to the ground-based radars where their measurements are more reliable (as it was noted by Smalley et al. 2017). However, overly restrictive distance-based filtering can lead to large statistical errors due to the insufficient sample

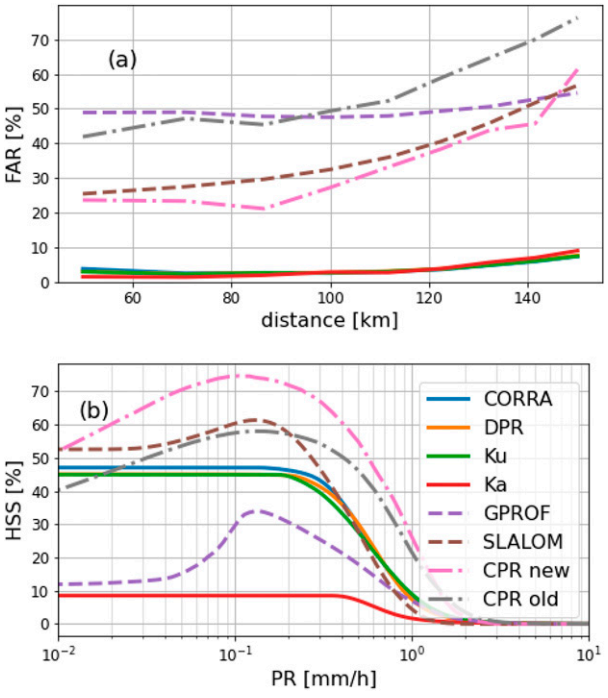

FIG. 4. (a) Dependence of the false alarm ratio on the distance to the nearest ground-based radar. (b) The HSS of the spaceborne algorithms as a function of the "no-snow" precipitation threshold. The color coding of the lines in (a) is given in (b).The "CPR-old" and "CPR-new" line represents the detection scores validated with the single-polarization and dual-polarization MRMS products, respectively. The single-polarization dataset spans from 2006 to 2011; the dual-polarization data cover the period from 2014 onward. Note that the DPR line is hidden below the Ku-only product's line.

size. Therefore, the analysis that follows is performed for all samples within 110 km from the ground-based radars.

The detection capabilities of the spaceborne sensors is assessed against the MRMS product, which has its own limitations. In principle, an instrument that is more sensitive than MRMS could detect snowfall where the reference indicates no-snow; such an occurrence would be misleadingly recorded as a false alarm. To address this issue, the sensitivity of each spaceborne retrieval is adapted to that of MRMS by introducing an algorithm-specific optimal filtering threshold (SB_{th}). Snowfall rates below SB_{th} are treated as "no-snow." In this way, low precipitation rates that are undetectable for MRMS, but not for the spaceborne product, are converted to "no-snow" in the spaceborne dataset. The threshold SB_{th} is identified by maximizing the Heidke skill score (HSS; Heidke 1926) over a range of precipitation rates. The HSS curves for each algorithm are shown in Fig. 4b. The PMW and *CloudSat* products display a well-defined peak at approximately 0.1 mm h^{-1} which confirms the legitimacy of the filtering procedure described above. The HSS curves of the DPR-based retrievals are flat for the precipitation rates below their sensitivity limit and then they gradually decrease. This indicates that no precipitation rate filtering is needed for these products as the spaceborne retrieval has an effective sensitivity that is not better than the reference. For consistency with the other algorithms, the sensitivity thresholds of the DPR is reported as the optimal threshold in Table 1.

To summarize, the detection capabilities of the spaceborne instruments are assessed for pixels within 110 km and where the probability of frozen precipitation according to the methodology of Sims and Liu (2015) exceeds 90%. Snowfall rates exceeding 21.3 mm h^{-1} and MRMS coarsened pixels that are less than 50% filled are not considered. The precipitation rates reported by the satellite retrievals that are below the SB_{th} are treated as "no-snow." For instance, a correct detection ("hit") is defined as a spaceborne sensor-resolution pixel for which at least 50% of the finer native resolution MRMS pixels are snow and the spaceborne estimate exceeds the intensity threshold given in Table 1. A correct rejection is triggered if MRMS reports no precipitation within the satellite footprint but the probability of snow exceeds 90% and the PR from the satellite is lower than the optimal threshold. Additionally, the quantitative comparison is performed where the upscaled MRMS pixels are not contaminated by rain and the spaceborne products also indicate frozen precipitation at the ground.

4. Results

a. *Detection of snow*

The detection capabilities of the spaceborne products is quantified in terms of the following metrics: the probability of

TABLE 1. Frozen precipitation detection scores over the analysis period for all surface types. CSI: critical success index; HSS: Heidke skill score; POD: probability of detection; FAR: false alarm ratio; SB_{th}: the threshold used for the spaceborne product to discriminate between "snow" and "no-snow" pixels in order to get the best agreement with the ground-based snow occurrences. The values in the parentheses for the *CloudSat* retrieval were obtained with the MRMS data prior to the dual-polarization upgrade for an earlier 5-yr period.

Score	SLALOM	GPROF	CORRA	DPR	Ku	Ka	2C-SNOW
POD (%)	57.3	28.1	32.9	31.1	31.0	4.8	78.4 (69.7)
FAR (%)	26.3	39.6	3.0	2.8	2.7	2.1	25.5 (47.0)
HSS (%)	58.7	31.3	47.1	45.1	45.0	8.5	74.7 (58.0)
CSI (%)	47.6	23.7	32.6	30.8	30.7	4.8	61.8 (43.1)
SB_{th} (mm h^{-1})	0.08	0.11	0.13	0.10	0.16	0.35	0.10 (0.14)
No. of MRMS "no-precipitation" samples	2 324 6950			8 945 928			225 355 (1 349 190)
No. of MRMS "snow" samples	1 869 954			745 312			16 003 (71 876)

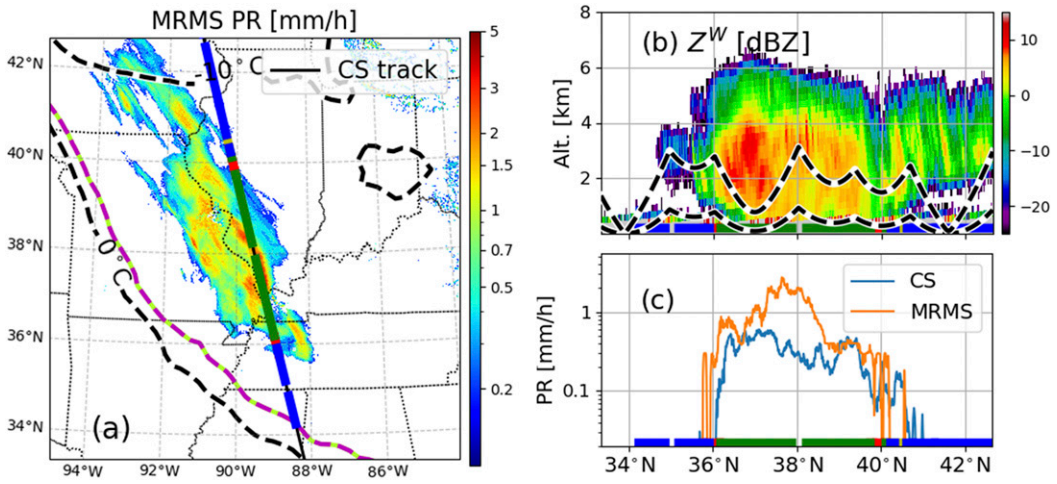

FIG. 5. (a) MRMS precipitation rates on 1918 UTC 10 Feb 2016. The thick dashed black lines mark the 2-m wet-bulb temperature isotherms of −10°, 0°, and 10°C. The magenta–green line indicates an edge of a region where probability of snow exceeds 90% according to the methodology of Sims and Liu (2015). State boundaries are shown as dotted lines. Different colors along the *CloudSat* track indicate correct rejections (blue), false alarms (yellow), missed detections (red), and hits (green) of the 2C-SNOW retrieval with respect to the MRMS product. (b) The corresponding *CloudSat* radar reflectivity. The black–white lines mark the top and the bottom of the lowest elevation scan of the NEXRAD radars; varying heights of these lines are the result of the varying distance from the *CloudSat* track to the nearest ground-based radar. (c) The collocated precipitation rates from 2C-SNOW (blue) and MRMS (orange) product along the *CloudSat* track. The color coding at the bottom of (b) and (c) corresponds to the detection capabilities of *CloudSat* shown in (a). The gaps in the data correspond to the points not included in the analysis due to fractional filling, high temperature, or distance to the ground-based radars.

detection (POD), the FAR, the HSS, and the critical success index (CSI). These measures are defined as

$$\mathrm{POD} = \frac{h}{h+m}; \quad \mathrm{FAR} = \frac{f}{f+r}; \quad \mathrm{CSI} = \frac{h}{h+f+m}; \tag{2}$$

$$\mathrm{HSS} = \frac{2(hr - fm)}{(h+m)(m+r) + (h+f)(f+r)}, \tag{3}$$

where h, f, m, and r denote the number of correct detections (hits), false alarms, missed detections, and correct rejections, respectively. A complete list of the detection scores is given in Table 1. The 2C-SNOW achieves by far the best performance in terms of CSI and HSS scores; 2C-SNOW exceeds an HSS of 75%, detects 3/4 of the snow events but triggers false alarms for 25% of the cases. Differences between the spaceborne and ground-based products occur mostly at the edges of storms (see an example in Fig. 5) where the spatial–temporal collocation procedure is less reliable. Some discrepancies between the snow detection algorithms are due to differences in the phase classification; e.g., *CloudSat* misses approximately 1% of precipitation events because it classifies them as rain and thus the 2C-SNOW algorithm provides no precipitation. The remaining differences between snow occurrences can be attributed to the blind zones of the instruments: all the spaceborne radars are generally affected by ground clutter in the first kilometer close to the ground (with worse performance over mountain regions), whereas the ground-based radars may overshoot shallow precipitation especially at far ranges and in the case of beam blocking (Smalley et al. 2017). This happens for the nonprecipitating part of the cloud at around 36°N in Fig. 5b; at this location, MRMS indicates "snow" because the lowest elevation scan of the ground-based radars samples in-cloud conditions rather than precipitation at the ground. Additionally, some of the disagreement between products can be attributed to the imperfection of the filtering methodology ($\mathrm{PR}_{\text{2C-SNOW}}$ values $< 0.10\,\mathrm{mm\,h^{-1}}$ are treated as "no-snow") as shown for few pixels around 40°N in Fig. 5 where both MRMS and 2C-SNOW indicate snowfall but missed detections are triggered because *CloudSat* reports very low precipitation rates.

The CORRA, Ku-only, and DPR products have similar detection capabilities (POD = 30%) which suggests that the precipitation detection is mainly driven by the Ku precipitation radar which is the most sensitive of the DPR pair (Battaglia et al. 2020), but still inadequate for snowfall studies. It was already shown by Skofronick-Jackson et al. (2019) that the DPR detects only 1/10 of the snow occurrences, compared to the *CloudSat* radar. They demonstrated that for this reason and due to differences between algorithms, the DPR reports only 1/3 of the snow accumulation. The sensitivity threshold of 12 dBZ of the Ku precipitation radar translates, via Eq. (1), to approximately $0.5\,\mathrm{mm\,h^{-1}}$ which explains the low detection skills. The Ka-only product performs worse than any of the retrievals under consideration. Again, the main issue affecting its detection capabilities is the sensitivity of the sensor (18 dBZ $\approx 1\,\mathrm{mm\,h^{-1}}$ in the matched swath) that results in only 6% of the snow events being captured.

TABLE 2. Frozen precipitation detection scores over different surface types, as derived from the Tool to Estimate Land Surface Emissivities at Microwave Frequencies (TELSEM).

Surface type	HSS (%)		POD (%)		FAR (%)		No. of MRMS pixels	
	SLALOM	GPROF	SLALOM	GPROF	SLALOM	GPROF	"No-snow"	"Snow"
Ocean	56.4	15.9	53.8	17.9	30.7	69.3	141 401	17 171
Sea ice	58.8	18.1	59.6	14.1	35.5	57.0	191 378	16 412
Maximum vegetation	59.5	34.4	50.1	23.1	21.6	20.0	1 836 370	98391
High vegetation	58.4	29.8	47.9	19.4	20.7	22.0	3 093 270	140 840
Moderate vegetation	60.0	28.0	48.7	17.4	17.7	14.3	1 137 098	46 667
Low vegetation	59.1	31.7	50.6	21.5	27.1	34.5	76 556	1528
Minimal vegetation	57.5	20.0	45.4	13.7	18.0	53.4	21 959	744
Maximum snow	56.4	12.0	64.9	23.0	46.0	85.3	613 511	35 924
Moderate snow	61.3	33.0	61.9	34.3	33.5	58.2	3 288 516	275 182
Low snow	59.7	31.4	59.7	27.9	34.2	52.3	2 966 481	244 867
Minimal snow	63.3	40.6	60.0	36.3	25.9	41.6	7 681 928	777 037
Standing water and rivers	57.4	26.7	46.3	18.3	17.8	35.0	444 285	27 356
Water/land coast boundary	59.1	21.7	52.0	13.9	22.4	16.0	1 597 261	167 793
Water/ice boundary	58.1	12.9	54.4	7.9	27.4	10.8	156 936	20 042

Out of the radiometer-based algorithms, SLALOM performs much better than GPROF (with double the GPROF HSS value) and DPR products, with HSS and CSI reaching 59% and 48%, respectively. These values are close to those of the CPR 2C-SNOW retrieval, the product it was trained on. This emphasizes that the GMI has a very high potential for snow detection, if trained with a high-sensitivity radar dataset. SLALOM is characterized by a much higher POD than the GPM radar products, but it is affected by a larger number of false alarms. The false detections mainly correspond to nonprecipitating ice clouds.

Out of all the products considered, GPROF suffers from the highest number of false alarms. This issue is related to the confounding effects of the background surface within the IFOV. Most of the false alarms are triggered over snow-covered land or sea ice where solid-phase water accumulated at the surface is confused with falling snow.

Because the brightness temperature measured by passive microwave radiometers depends on the emissivity of the background surface, an analysis of the detection capabilities of the radiometric products over different surface types was performed. We use the same land classification scheme that is adopted in the GPROF algorithm, where a *K*-means clustering of emissivities is exploited to define 10 self-similar surface types, ranging from different vegetation types to snow-covered surfaces and inland water pixels. For more detail on the classification methodology, see Aires et al. (2011).

The HSS score of the SLALOM algorithm is relatively stable irrespective of the surface type and it varies between 56% over "maximum snow" and 63% for the "minimal snow" (see Table 2). There is not much difference in terms of HSS between vegetated land and snow-covered surfaces. Nevertheless, FAR is larger for all the snow-covered surface types and sea ice compared to vegetation (25%–45% versus 20%–30%). This indicates the difficulties that the PMW instruments encounter in distinguishing between the snowfall and the snow at the ground.

The GPROF product exhibits a much greater dependence of the HSS on the surface type, as opposed to SLALOM. There is almost a factor of 3 difference between the lowest and the highest HSS over the different surfaces. The lowest HSS (≤15%) is reported over "maximum snow," "water/ice boundary," "sea ice," and "ocean," all of which (except for "ocean") are associated with snow/ice cover. The low performance of the algorithm over the ocean is difficult to interpret. On the one hand, it may reflect poor sampling due to limited MRMS coverage of the ocean cases, almost entirely at longer ranges. On the other hand, the SLALOM algorithm is not affected by this issue, which suggests at deficiencies of the GPROF retrieval. Note that snow cover cannot be unambiguously related to the poorer detection capabilities of GPROF. Moderate, low, and minimal snow classes perform comparably to different vegetation types in terms of HSS but, as for SLALOM, they are associated with an elevated FAR. Interestingly, the poor performance of the two worst classes is the effect of different mechanisms. On one hand, over "water/ice boundaries," both the POD and FAR are very low (8% and 11%, respectively), which indicates a very conservative detection procedure. On the other hand, for the "maximum snow" class, the FAR is the highest among all the surface types which suggests a completely opposite approach. Nevertheless, the GPROF algorithm still produces many missed detections on snow-covered surfaces, as shown in Fig. 6. Note that the POD over snow-covered surfaces in the GPROF product in general is higher than over the other surface types. This might be the result of using different precipitation datasets to construct the a priori database (see section 2b(3)) with the DPR-based products being used over all surface types except for those covered in snow. Even a visual comparison between the number of correct snow detections in the March 2017 North American blizzard (Figs. 6e,f) confirms the better performances of SLALOM over GPROF in mapping snow, irrespective of the surface type.

b. *Probability distribution functions of snow occurrences*

The first qualitative comparison of the products is shown in Fig. 7, where the probability distribution functions (PDF) of the snow intensity are presented. All of the PDFs include

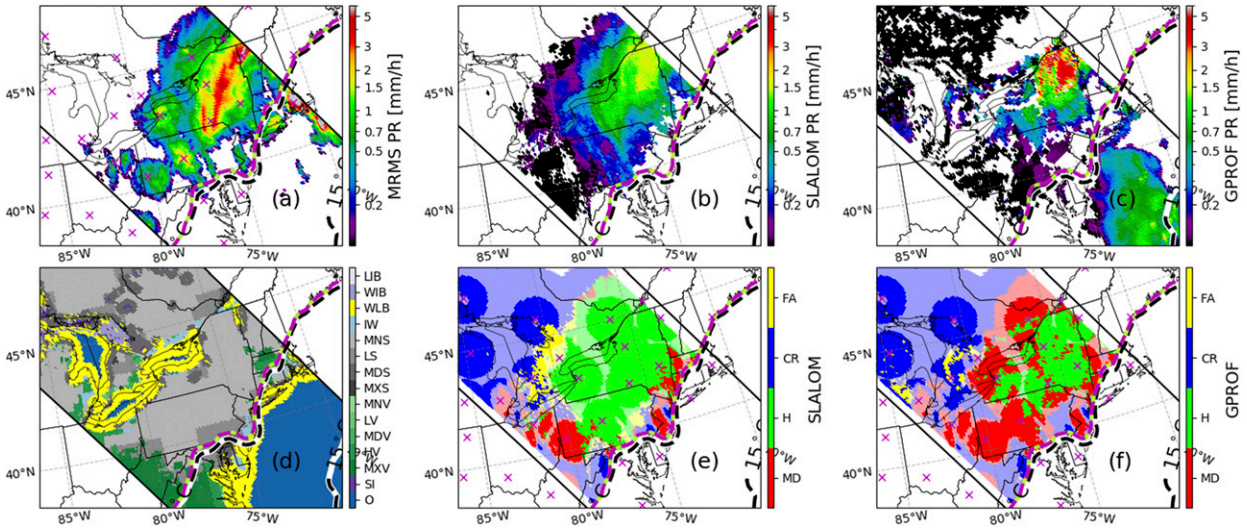

FIG. 6. The 14 March 2017 case study. (a)–(c) Precipitation rate at the GMI 36-GHz channel resolution from MRMS, SLALOM and GPROF, respectively. (d) Surface type classification including ocean (O), sea ice (SI), maximum vegetation (MXV), high vegetation (HV), moderate vegetation (MDV), low vegetation (LV), minimal vegetation (MNV), maximum snow (MXS), moderate snow (MDS), low snow (LS), minimal snow (MNS), standing water and rivers (IW), water/land boundary (WLB), water/ice boundary (WIB), and land/ice boundary (LIB). (e),(f) Snow detection scores, i.e., the false alarms (FA), correct rejections (CR), hits (H), and missed detections (MD) over the points that satisfy all the criteria for the comparison. Faint colors indicate points that are further than 110 km from the MRMS radars and are not used in the statistical analysis. The magenta crosses show the radar locations. The thick dashed black lines mark the 2-m wet-bulb temperature isotherms of 0° and 15°C. The magenta–yellow line indicates the edge of the region where probability of snow exceeds 90% according to the methodology of Sims and Liu (2015).

precipitation rates below the respective spaceborne optimal threshold and are normalized such that the area under each curve is unity (the spike at the bin $[0, 10^{-3}]$ mm h^{-1} is truncated). Despite differences in the spatial resolution of the CPR-, DPR- and GMI-based products, the distributions of the coarsened MRMS precipitation rates (blue lines) are very similar, an indication that NUBF does not have a huge impact over the CONUS. Note that this may not be the case over ocean, where snowfall originated in shallow convective systems is more likely to occur (Kulie et al. 2016). The number of heavy snowfall events decreases exponentially with their intensity. A rapid increase in the number of small PR cases ($0.1 < \text{PR} < 0.3$ mm h^{-1}) is associated with the construction of the dataset, i.e., to the 50% IFOV filling constraint combined with the sensitivity threshold of the MRMS (0.2 mm h^{-1}) and some smoothing introduced by the spatial coarsening procedure. The high sensitivity of the CPR reveals that the MRMS product clearly underestimates the number of light snowfall events (PR < 0.2 mm h^{-1}). On the other hand, issues related to the reduced backscattering efficiency at W band and to the attenuation correction in heavier snow events (Matrosov and Battaglia 2009; Cao et al. 2014; Battaglia and Panegrossi 2020) causes underestimation of the highest precipitation rates (exceeding 1.5 mm h^{-1}) in the CloudSat product. The sensitivity issue of the DPR radar, discussed in the previous section, is very clear in the PDFs with precipitation rates below 0.1 mm h^{-1} (0.3 mm h^{-1}) almost nonexistent in CORRA, DPR and Ku-only (Ka-only) products. All the radar-based algorithms clearly underestimate the snowfall rates at the ground. The radar–radiometer, DPR, and Ku-only retrievals produce very similar PDFs which indicates that the Ku Precipitation Radar data are the backbone of all these three algorithms. All of the spaceborne products are characterized by a lower number of snow events exceeding 0.2 mm h^{-1} (1 mm h^{-1} for 2C-SNOW) than the ground-based reference, which suggests their tendency to underestimate the snowfall rates.

c. *Quantitative snow estimates*

Figure 8 provides a more detailed comparison between the MRMS and spaceborne retrievals. Due to the similarities between the CORRA and Ku-only products, only the former is shown. The two-dimensional data clearly indicate that all of the spaceborne snowfall algorithms considered here tend to underestimate precipitation rates with 2C-SNOW being the closest to the 1–1 line. The radar–radiometer combined product (CORRA) is almost identical to the radar-only retrieval (DPR), which indicates a minimal impact of the radiometric data on the final precipitation rate estimate over land. The two-dimensional PDFs of the radiometer-only algorithms (SLALOM and GPROF) are characterized by more spread along the y axis, which indicates an increased uncertainty of these products.

The precision and accuracy of satellite snowfall retrievals is quantified by the following metrics: the mean error (ME), the root-mean-square error (RMSE), the mean fractional absolute error (MFAE), and the multiplicative bias (MB) defined as

$$\text{ME} = \frac{1}{N}\sum_{i=1}^{N}(\text{PR}_{\text{SB}} - \text{PR}_{\text{MRMS}}), \tag{4}$$

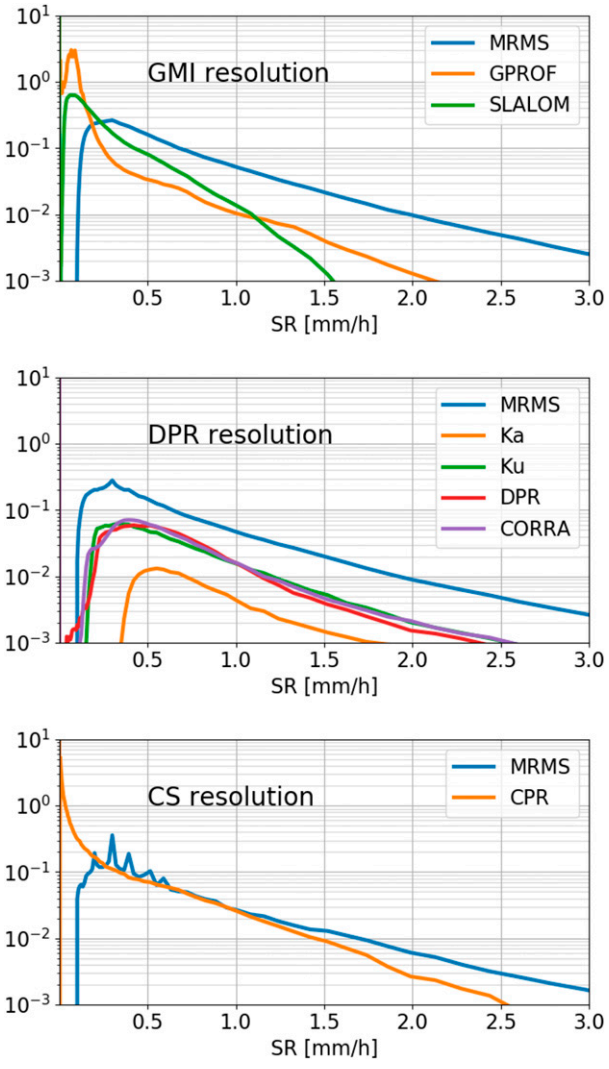

FIG. 7. Probability distribution functions of the snowfall rate occurrence. Different panels correspond to the different horizontal resolutions of the spaceborne instruments. All of the PDFs include nonprecipitation pixels for ease of comparison.

$$\mathrm{RMSE} = \sqrt{\frac{1}{N}\sum_{i=1}^{N}(\mathrm{PR}_{\mathrm{SB}} - \mathrm{PR}_{\mathrm{MRMS}})^2}, \tag{5}$$

$$\mathrm{MFAE} = \frac{1}{N}\sum_{i=1}^{N}\frac{|\mathrm{PR}_{\mathrm{SB}} - \mathrm{PR}_{\mathrm{MRMS}}|}{\mathrm{PR}_{\mathrm{MRMS}}}, \tag{6}$$

$$\mathrm{MB} = \frac{\sum_{i=1}^{N}\mathrm{PR}_{\mathrm{SB}}}{\sum_{i=1}^{N}\mathrm{PR}_{\mathrm{MRMS}}}. \tag{7}$$

Table 3 summarizes the bulk statistics of the snow products under consideration. Comparison between the retrievals is performed on the data points where both the satellite and MRMS indicates snow at the ground and the spaceborne estimators exceed their optimal detection thresholds shown in Table 1; i.e., only the points above the black solid line in Fig. 8 are considered. The comparison of the 2C-SNOW algorithm is performed with the MRMS dataset that combines the single-polarization (2006–11) and the dual-polarization quality-controlled (2016–17) products.

It is evident that the 2C-SNOW retrieval outperforms the other spaceborne products. It is characterized by the best ME, RMSE and MB. The Ku-only and the GPROF algorithms are the leaders for the remaining two categories, i.e., the CC and the MFAE, respectively. The mean error of the 2C-SNOW retrieval reported in this study ($-0.19\,\mathrm{mm\,h^{-1}}$) matches the $0.19\,\mathrm{mm\,h^{-1}}$ value derived by Cao et al. (2014), where a similar analysis was performed over the period from January 2009 to March 2011. Our RMSE is slightly larger than in their analysis (0.71 versus $0.46\,\mathrm{mm\,h^{-1}}$). These small differences may arise from the filtering of the low precipitation rates of the *CloudSat* product adopted in this study. In terms of the RMSE, the Ka-only retrieval is characterized by the largest error ($1.5\,\mathrm{mm\,h^{-1}}$), GPROF achieves slightly better results with RMSE of $1.1\,\mathrm{mm\,h^{-1}}$ while the DPR, Ku-only and CORRA retrievals are characterized by RMSE of $0.9\,\mathrm{mm\,h^{-1}}$. SLALOM with the score of $0.77\,\mathrm{mm\,h^{-1}}$ ranks at the second place just behind 2C-SNOW. All of the products tend to underestimate snowfall rates at the ground which is reflected in the negative mean error values. Again, 2C-SNOW and SLALOM are the least biased. In terms of the total precipitation amount, 2C-SNOW generates 78% of the MRMS values. The DPR, Ku-only, and CORRA products correspond to an MB of approximately 53%, while the radiometer-based retrievals are characterized by larger underestimation with multiplicative biases of around 49% for SLALOM and 41% for GPROF. For SLALOM, this is mainly caused by a severe underestimation of the highest precipitation rates. GPROF underestimates PR over the whole range of snowfall intensities. A MB of the Ka-only is comparable to the one of GPROF. All of the satellite products are characterized by moderate correlation coefficient values ranging from 0.3 for the Ka-only to 0.49 for the Ku-only products, which reflects the high degree of uncertainty in snowfall estimates.

The accuracy and the precision results derived for SLALOM and GPROF algorithms seem to be worse than those obtained by Meng et al. (2020) for the Advanced Microwave Sounding Unit-A (AMSU-A) and MHS pair and the ATMS. These PMW cross-track scanning sounders have channels with a similar frequency range to the GMI, i.e., from 23.8 GHz to 190.31 GHz (MHS)/183.31 GHz (ATMS). Their physical algorithm is characterized by a mean error of $-0.15\,\mathrm{mm\,h^{-1}}$ and a RMSE of $0.63\,\mathrm{mm\,h^{-1}}$. Such results are not observed even for the 2C-SNOW product which suggests that the analysis of Meng et al. (2020), unlike the analysis in Table 3, may have included pixels considered to be nonprecipitating in this study. By mimicking their approach, i.e., by considering all coarsened "snow" and "no-snow" MRMS samples, the RMSE of both SLALOM and GPROF is brought down to $0.33\,\mathrm{mm\,h^{-1}}$, while the ME is reduced to -0.05 and $-0.06\,\mathrm{mm\,h^{-1}}$, respectively.

d. Calibration with MRMS

The snow climatology provided by spaceborne products differs noticeably from the ground-based reference. Clearly,

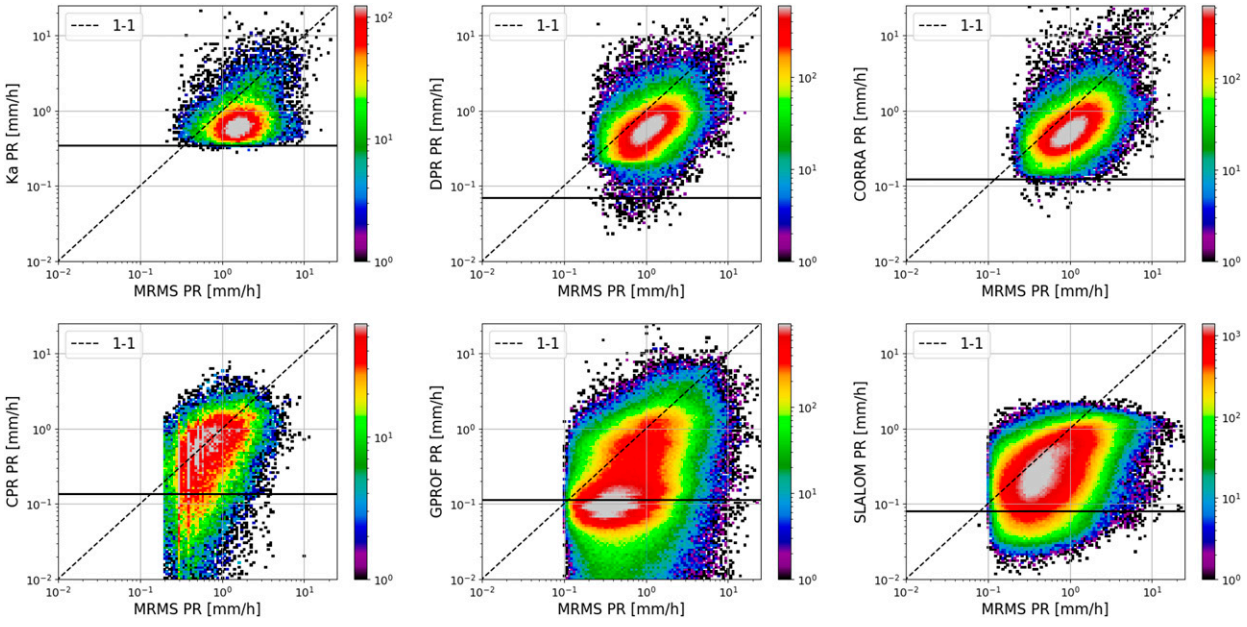

FIG. 8. Two-dimensional histograms of the snowfall validation dataset. The x axis represents the ground-based reference dataset; the y axis corresponds to the spaceborne product. (top) The Ka-only, DPR, and CORRA retrievals. (bottom) The 2C-SNOW, GPROF, and SLALOM algorithms. Data are binned using logarithmic spacing on both axes. The black dashed line indicates the 1–1 correspondence. The horizontal, black, solid line show the limit on the spaceborne algorithms that optimizes the precipitation detection matching with MRMS.

this is related to the low temporal sampling, limited swath sizes and sensitivity issues of the DPR radar, but it is also the result of diverse microphysical assumptions made by different retrievals such as variable snow densities, falling-velocity assumptions and so on. Such discrepancies in the algorithms result in systematic differences between the snowfall estimates, which is reflected in e.g., the multiplicative bias values diverging from 1. Following the methodology of Meng et al. (2020), this effect is mitigated by calibrating the spaceborne products with MRMS over the snowing pixels. First, the validation dataset is split into training and verification periods. The training is performed with the last year of data. The products are calibrated by minimizing the RMSE between the MRMS precipitation rates and a third-order polynomial of the spaceborne estimate:

$$\mathrm{PR}_{\mathrm{SB}}^{C} = \sum_{n=1}^{3} p_n \mathrm{PR}_{\mathrm{SB}}^{n}, \tag{8}$$

where $\mathrm{PR}_{\mathrm{SB}}^{C}$ denotes the corrected spaceborne precipitation rate, p_n are the fitting parameters, and $\mathrm{PR}_{\mathrm{SB}}$ is the original satellite precipitation rate. Note that the polynomial has no constant term. The optimal coefficients of the polynomial derived for each product along with the precision scores (in the parenthesis) are given in Tab 3. By design, this methodology improves the RMSE and, as a result, the mean error and the

TABLE 3. Frozen precipitation precision metrics for pixels where MRMS detects pure snow that fills at least half of the spaceborne IFOV and the spaceborne product exceeds the precipitation threshold given in Table 1. The considered metrics include the following: ME—mean error; RMSE—root-mean-square error; MFAE—mean fractional absolute error; MB—multiplicative bias; CC—correlation coefficient. The terms p_3, p_2, and p_1 are the coefficients of the polynomial $\sum p_n \mathrm{PR}_{\mathrm{SB}}^{n}$ that minimizes RMSE between MRMS and the spaceborne product. The scores for the retrievals calibrated with MRMS are in parentheses.

	SLALOM	GPROF	CORRA	DPR	Ku	Ka	2C-SNOW
ME (mm h^{-1})	−0.44 (−0.04)	−0.68 (−0.18)	−0.57 (−0.02)	−0.59 (0.02)	−0.58 (−0.01)	−1.10 (0.12)	−0.19 (−0.02)
RMSE (mm h^{-1})	0.77 (0.67)	1.14 (0.89)	0.92 (1.00)	0.93 (1.01)	0.90 (0.94)	1.52 (1.10)	0.71 (0.63)
MFAE (%)	49.0 (59.0)	60.1 (58.6)	48.8 (48.1)	49.2 (48.8)	50.8 (44.0)	56.5 (54.3)	55.5 (61.8)
MB (%)	48.9 (95.7)	41.3 (83.3)	53.1 (98.6)	52.5 (101.4)	53.1 (99.4)	41.5 (106.4)	78.2 (97.5)
CC	0.39 (0.37)	0.37 (0.35)	0.41 (0.35)	0.39 (0.34)	0.49 (0.46)	0.30 (0.19)	0.37 (0.36)
No. of "hits"	1 020 734	141 744	218 277	208 914	208 410	28 072	48 086
p_3	1.18	0.04	0.01	0.02	0.01	0.03	0.09
p_2	−2.98	−0.56	−0.26	−0.43	−0.24	−0.66	−0.77
p_1	3.19	2.14	1.90	2.33	1.89	3.10	1.90

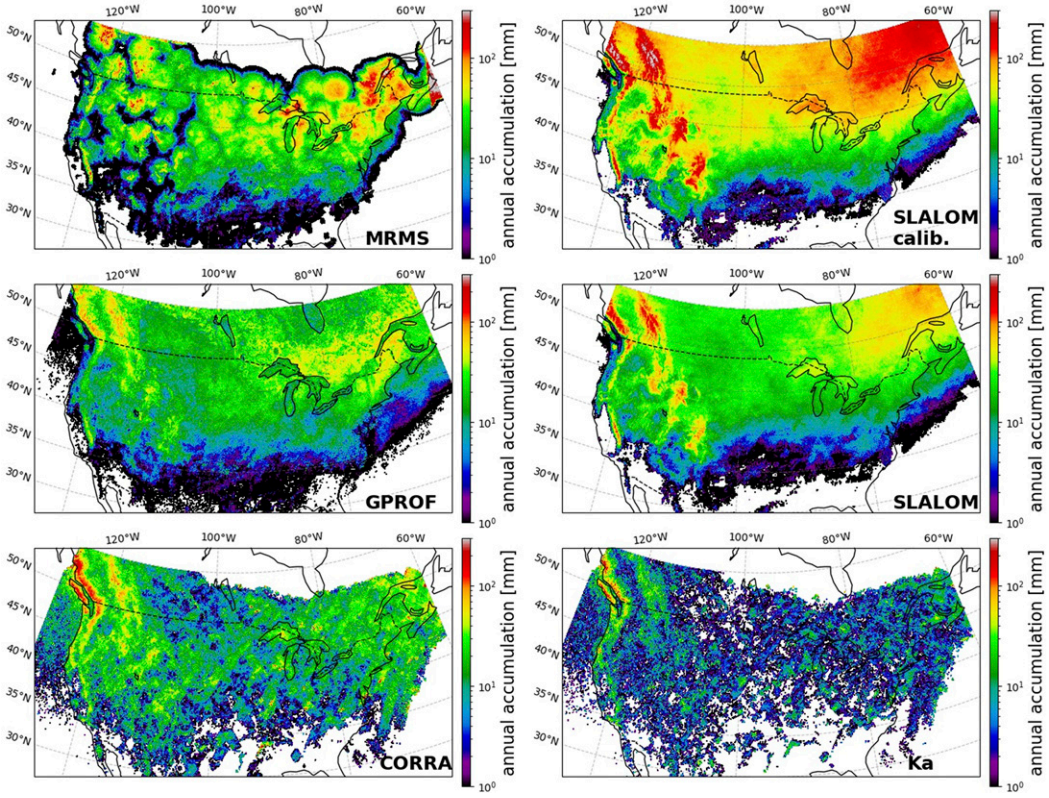

FIG. 9. Mean annual snowfall accumulation over the 4-yr period (2016–19) restricted to the GPM coincident scans for several products analyzed as indicated by the labels in the bottom-right corner. The data are binned into 0.1° × 0.1° regions. The accumulation for the MRMS and GPROF products are computed for the pixels where the frozen fraction exceeds 90% (see discussion in section 3). The Ka-only and CORRA retrievals are accumulated over profiles where snow is detected in the lowest clutter free radar bin. The "SLALOM calib." product shows the climatology of the SLALOM algorithm calibrated with the MRMS data at close ranges following the procedure of Meng et al. (2020).

multiplicative bias that approach the best possible scores (ME = 0 mm h^{-1} and MB = 100%) for all of the products except for GPROF and Ka only. The lower improvement for these retrievals can be attributed to the statistical noise in the Ka-only algorithm and heterogeneous training dataset of GPROF (Fig. 8). The correlation coefficients for each product show no improvement after calibration to MRMS. Given the ease of application of the polynomial correction, this methodology can be successfully applied to PMW algorithms to produce a global snow climatology that is more consistent with the radar measurements. SLALOM seems to be the best suited for testing these results because of its high detection capabilities and its substantially improved multiplicative bias value after the calibration.

e. *Annual snow accumulation over the United States*

The spatial distribution of the mean annual snow accumulation derived from 4 full years of data (2016–19) for some of the products analyzed here is shown in Fig. 9. To calculate the mean annual accumulation, the analysis domain is split into 0.1° × 0.1° boxes. Then, a mean snowfall rate in each latitude–longitude box is computed for the MRMS data upscaled to the GMI resolution. The MRMS data have been previously matched in space, time, and resolution with each satellite footprint. The same procedure is repeated for the spaceborne products at their native pixel size. Next, the average snowfall rate is multiplied by 24 (hours) and 365 (days). In this way, the average annual accumulation is computed subject to being observed by the GMI. Despite differences in the beam size, the sampling resolution, and the swath width of the different instruments, the mean precipitation rate in the latitude–longitude box should converge to the same value if the sample size is large enough. The snow accumulation of the MRMS product is calculated using pixels where frozen precipitation represents at least 90% of the total precipitation area within the GMI FOV. The same frozen fraction threshold is also used for the GPROF retrieval; i.e., the total accumulation is calculated only over pixels where the ratio between the frozenPrecipitation and mostLikelyPrecipitation GPROF products exceeds 90%. In the case of the Ka-only and the CORRA algorithms, only the data that are flagged as ice above the lowest clutter free ranges are used.

The effect of signal blockage is very clear in the MRMS data (Kirstetter et al. 2012), especially over the Rocky

Mountains, where regions of very little snow amounts are adjacent to those where the accumulation exceeds 30 mm and more (Smalley et al. 2017). Moreover, circular patterns of enhanced snow amount, mostly present at the north edge of the MRMS domain, show that the product quality degrades with the range from the ground-based radars, a feature already discussed in section 3. Both of these factors seriously hinder MRMS-V11-based climatological studies of the snow spatial distribution, its impact on the water cycle, hazard analysis related to the snowfall intensity and, last but not least, the analysis of the expected rise in the river levels during spring. The GPM-DPR products are free of the aforementioned issues and therefore they provide complementary information on the snowfall distribution in the orographic areas and at far ranges. For instance, they reveal a band of large snow accumulation over and east of Vancouver Island that is not present in the MRMS data. However, the presented DPR-based algorithms largely underestimate the accumulation, with the Ka-only product being the most affected. Moreover, because of their limited sensitivity, the climatology they provide is biased toward heavy snowfall events and it results in a very patchy picture due to their low probability of detection. The climatology based on the PMW products presents the most consistent picture of snowfall, but it is not free from drawbacks. For instance, there is a sharp contrast between the precipitation amounts nearby and over the Great Lakes and the Hudson Bay in the GPROF retrieval. This behavior can be related to the different a priori databases used over ocean, snow/ice, and land for the algorithm training. This issue does not affect the climatology of SLALOM. In general, the spatial distribution of snow is similar in both PMW algorithms with SLALOM providing higher snowfall estimates that are closer to, but still lower than, the MRMS product near the ground-based radars, e.g., close to Quebec City in Canada.

The MRMS-calibrated climatology of SLALOM snow accumulation (see section 4d) is shown in the top-right panel of Fig. 9. Clearly, it provides higher snow accumulation values than any other spaceborne algorithm. It agrees better with the ground-based product, especially in proximity to the radars. Unfortunately, the lack of reliable ''ground-truth'' data over the Rocky Mountains preclude the verification as to whether the high amount of precipitation reported there is real or it corresponds to false alarms over the snow-covered mountains. Consequently, the availability of dense precipitation gauge networks in regions where ground-based radars have limited coverage (due to signal blockage) is of paramount importance for validating remote-sensor-derived precipitation products, especially those retrieved from spaceborne sensors (Derin et al. 2016; Navarro et al. 2019)

f. The effect of supercooled cloud droplets

One of the features of the SLALOM retrieval is a supercooled droplets detection (SCDD) module at the cloud tops. This module is based on a random forest approach, with the training dataset excluding any embedded supercooled droplet cases. The *CloudSat*/*CALIPSO*-based training dataset contains 397 033 observations: 10 783 snowfall cases without supercooled droplets and 16 327 snowfall cases with supercooled droplets at cloud top. The SCDD module is similar to the SLALOM snow detection model, with the same input variables, i.e., T2m, TPW, the vertical profiles of temperature, specific humidity, relative humidity, and all 13 GMI channels. The final forest consists of 300 decision trees and it outputs a probability of supercooled droplet occurrence at the GMI sampling locations. Validation of the SCDD module proves its high accuracy, with a POD of 97%, a FAR of only 5%, and an HSS reaching 89% (Rysman et al. 2018). We use this detection capability to assess their impact on the accuracy of PMW retrievals. For this purpose, the validation data are split according to the presence of supercooled particles (Fig. 10). The emissivity effect of liquid water is visible in both products, with both tending to underestimate the precipitation rates to a greater extent when supercooled droplets are present within the IFOV. This finding is more pronounced in the GPROF algorithm, where clouds with the supercooled droplet layer at the top rarely exceed precipitation rates of 0.2–0.3 mm h^{-1}. This results in a notable decorrelation of the ground-based and spaceborne products (CC = 0.16). Moreover, the multiplicative bias for mixed-phase clouds is more than 2 times worse than for ice-only (24% versus 57%; note that 1 is the perfect score). SLALOM seems to be less affected, nevertheless its accuracy is also degraded by a factor of 2 in terms of the MB (33% versus 61%) when supercooled droplets are present at the cloud top. Since SLW is mostly associated to low snow rates, the overall accuracy of the PMW products is not strongly affected, as shown in Rysman et al. (2019).

5. Summary and conclusions

This study compares various GPM and *CloudSat* snowfall products to the MRMS precipitation data over the continental United States during the period from November 2014 to September 2020. The following retrievals were analyzed: three based on the GPM radar-only measurements (Ka-only, Ku-only, and DPR products), the GPM combined radar–radiometer algorithm (CORRA), two passive microwave retrievals (GPROF and SLALOM), and the 2C-SNOW *CloudSat* radar product. The ground-based reference data were spatially and temporally matched in resolution to each spaceborne retrieval prior to the analysis.

Among the algorithms tested here, the 2C-SNOW product exhibits the best performances in terms of snowfall detection. When assessed with the dual-polarization quality-controlled MRMS data, 2C-SNOW has an HSS score of almost 75%, detects 75% of snow events, and falsely issues an alarm for only one in four cases. The discrepancies between MRMS and 2C-SNOW arise mainly from the problems with sensing close to the surface, i.e., *CloudSat* measurements are affected by the ground clutter whereas the altitude of the ground-based measurements increases progressively with the distance from the sensor, which creates a blind zone close to the ground.

The Ka-only product ranks at the other end of the spectrum of the snowfall detection capabilities, with an HSS of approximately 9%. The main issue affecting its performance is the sensitivity limit of the sensor (18 dB$Z \approx 1$ mm h^{-1}) that results

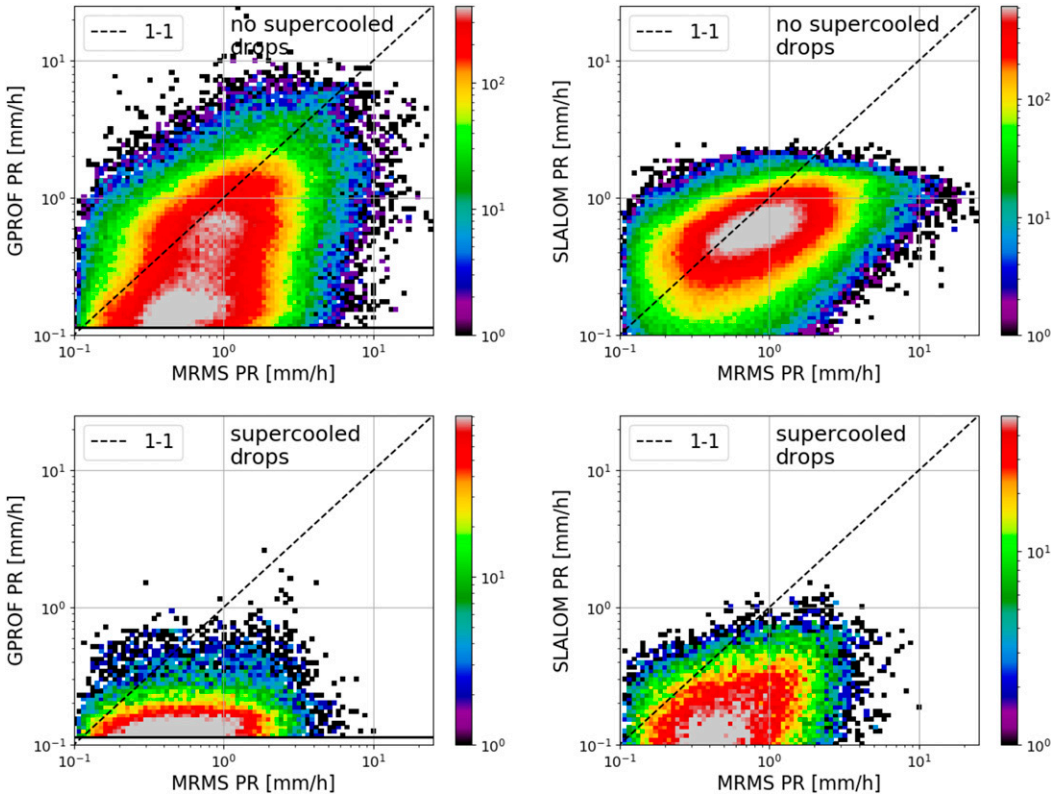

FIG. 10. Two-dimensional histograms of the snowfall intensity for the systems (bottom) with and (top) without supercooled droplets identified at the cloud top by SLALOM. The (left) GPROF and (right) SLALOM algorithms.

in only 5% of snowfall identified by MRMS being captured. The same problem, but to a lesser degree, applies to the Ku-only, DPR, and CORRA products. Their detection skills are limited by the sensitivity of the Ku module of the DPR system. With the ability to detect radar targets of 12 dBZ, all of these algorithms identify approximately 30% of solid precipitation occurrences. This combined with a very low false alarm rate (FAR; below 3%) increases the HSS to 45%.

The PMW products tend to detect more snowfall events than the DPR retrievals but they also trigger more false alarms. The analysis of almost 6 years of collocated PMW and ground-based snowfall estimates shows the advantages of *CloudSat*/*CALIPSO*-based machine learning retrievals [SLALOM and similar approached proposed by Liu and Seo (2013) and Kongoli et al. (2015)] over the traditional physically based approaches (GPROF), with HSSs of 59% versus 31%, respectively. The performance of the machine learning algorithm is only 15 percentage points worse than that of the CPR 2C-SNOW retrieval (albeit with a much larger sample), the product it was trained on. This shows the great potential of artificial intelligence solutions to improve the quality of precipitation retrieval algorithms, as long as the training is based on high quality data. Notably, GPROF's worse results may also result from the a priori dataset used in the Bayesian approach, which is based on GPM DPR products that suffer from low radar sensitivity and poor snow detectability. The performance of the PMW retrievals strongly depends on the surface type within the IFOV. In particular, the number of false alarms over snow-covered surfaces is 2–3 times larger than over vegetated areas. In the most extreme case of surfaces covered with deep snow, the false alarm ratio reaches 46% and 85% for SLALOM and GPROF, respectively. The same quantity over vegetation covered land covered does not exceed 20% and 30%, respectively.

All of the spaceborne products analyzed here tend to underestimate the intensity of the snowfall events. The snow accumulation for the correct detections in all the GPM algorithms is only one-half of the MRMS values (multiplicative bias of 50%). This is a serious issue for quantifying snowfall and for the Earth energy budget studies, especially for those based on the GPM-DPR products that are additionally affected by an abundant number of missed detections, as already noted by Skofronick-Jackson et al. (2019). The *CloudSat* 2C-SNOW algorithm is in better agreement with the ground-based product; it is also affected by some underestimation of the precipitation accumulation over correctly detected events due to high-end reflectivity saturation, but the bias is less pronounced (multiplicative bias of 80%, i.e., 20% underestimation).

Furthermore it is shown that, by calibrating the spaceborne products with the reference data, the systematic bias can be effectively reduced to almost zero. The polynomial correction proposed in this study has a positive impact on almost all of the metrics used to measure the agreement with the reference MRMS product, apart from the correlation coefficient.

Despite its limited sampling capability, the *CloudSat*-CPR provides by far the most complete view of snow systems (both in terms of snow occurrences and of snow PDF), with limited capabilities only when quantifying intense snowfall rate, due to the well-known saturation of W-band reflectivities in the presence of centimeter-size non-Rayleigh targets and issues related to the attenuation correction. The GPM-DPR offers better coverage and is certainly more valuable for medium/heavy snow conditions. However, the low DPR minimum sensitivity (around 12 dBZ at Ku band) seriously hampers DPR snowfall detection and quantitative estimates. The two PMW products considered here (GPROF and SLALOM) outperform the DPR retrievals; they generally underestimate the total amount of snowfall with a tendency to underestimate large snow rates. However, the calibration proposed in this study can effectively reduce this issue. Our analysis also suggests a better performance from SLALOM, which is trained by the global A-Train (*CloudSat* and *CALIPSO*) observations.

The snowfall results presented in this study are substantially worse than those obtained for liquid precipitation over the CONUS by Kidd et al. (2018), with the DPR-Ku product biased marginally low (ME = $-0.04\,\mathrm{mm\,h^{-1}}$) and GPROF biased slightly high (ME = $0.15\,\mathrm{mm\,h^{-1}}$). In their study, both algorithms exhibited high POD (>70%), high HSS of 0.77 and 0.67, and CC exceeding 0.61 and 0.55 for the radar and the radiometer products, respectively. These results confirm that the retrievals of snow are much more challenging than those of rain; more research is needed to constrain the underlying uncertainties and dedicated spaceborne missions targeting snow and high-latitude precipitation are highly recommended (Battaglia et al. 2020). Such developments will be paramount toward providing a better characterization of Earth's energy and water budget.

Acknowledgments. This research used the ALICE High Performance Computing Facility at the University of Leicester. The work by Kamil Mroz was performed at the University of Leicester under contract with the National Centre for Earth Observation. The project was supported by the European Space Agency under the activity "RainCast," Contract 4000125959/18/NL/NA and by the EUMETSAT "Satellite Application Facility on Support to Operational Hydrology and Water Management" (H SAF) Third Continuous Development and Operations Phase (CDOP-3). Pierre Kirstetter acknowledges support through the NASA Precipitation Measurement Missions Award 80NSSC19K0681 and the NASA Ground Validation Program Award NNX16AL23G. The GPM data were provided by the NASA Goddard Space Flight Center and PPS, which develop and compute the DPR, Ku, Ka, CORRA, and GPROF precipitation datasets as a contribution to GPM and archived at the NASA GES DISC. The authors express their sincere gratitude to Daniele Casella, Andrea Camplani, and Paolo Sanò (at CNR-ISAC) for their work within the RainCast project on SLALOM retrieval and to Jean-François Rysman (LMD, France) for his work during SLALOM development and his guidance. The authors thank Joe Turk (NASA JPL) for supporting and promoting this study within the NASA Precipitation Measurement Mission (PMM) Science Team. Thanks to Daniel Watters for proofreading the article.

Data availability statement. The MRMS version 11 data used in this study are stored by the Department of Geological and Atmospheric Sciences at Iowa State University and the Open Science Data Cloud at http://mtarchive.geol.iastate.edu/YYYY/MM/DD/mrms/ncep/. The single polarization MRMS precipitation product is available at https://doi.org/10.25638/EDC.PRECIP.0001. The GPM DPR V06 data archived at the NASA GES DISC are openly available at the following locations: doi:10.5067/GPM/DPR/GPM/2A/06, doi:10.5067/GPM/DPR/Ka/2A/06, doi:10.5067/GPM/DPR/Ku/2A/06, doi:10.5067/GPM/DPRGMI/CMB/2B/06. The GPROF V05 product is stored at doi:10.5067/GPM/GMI/GPM/GPROF/2A/05. The *CloudSat* 2C-SNOW product can be freely downloaded from ftp.cloudsat.cira.colostate.edu/2C-SNOW-PROFILE.P1_R05. The SLALOM algorithm is not operational yet but the data that support the findings of this study are available on request from the corresponding author, KM.

REFERENCES

Aires, F., C. Prigent, F. Bernardo, C. Jiménez, R. Saunders, and P. Brunel, 2011: A Tool to Estimate Land-Surface Emissivities at Microwave Frequencies (TELSEM) for use in numerical weather prediction. *Quart. J. Roy. Meteor. Soc.*, **137**, 690–699, https://doi.org/10.1002/qj.803.

Battaglia, A., and G. Panegrossi, 2020: What can we learn from the CloudSat radiometric mode observations of snowfall? *Remote Sens.*, **12**, 3285, https://doi.org/10.3390/rs12203285.

——, and Coauthors, 2020: Spaceborne cloud and precipitation radars: Status, challenges, and ways forward. *Rev. Geophys.*, **58**, e2019RG000686, https://doi.org/10.1029/2019RG000686.

Bauer, P., and R. Bennartz, 1998: Tropical Rainfall Measuring Mission microwave imaging capabilities for the observation of rain clouds. *Radio Sci.*, **33**, 335–349, https://doi.org/10.1029/97RS02049.

Bennartz, R., and P. Bauer, 2003: Sensitivity of microwave radiances at 85–183 GHz to precipitating ice particles. *Radio Sci.*, **38**, 8075, https://doi.org/10.1029/2002RS002626.

——, F. Fell, C. Pettersen, M. D. Shupe, and D. Schuettemeyer, 2019: Spatial and temporal variability of snowfall over Greenland from CloudSat observations. *Atmos. Chem. Phys.*, **19**, 8101–8121, https://doi.org/10.5194/acp-19-8101-2019.

Cao, Q., Y. Hong, S. Chen, J. J. Gourley, J. Zhang, and P. E. Kirstetter, 2014: Snowfall detectability of NASA's CloudSat: The first cross-investigation of its 2C-SNOW-PROFILE product and National Multi-Sensor Mosaic QPE (NMQ) snowfall data. *Prog. Electromagn. Res.*, **148**, 55–61, https://doi.org/10.2528/PIER14030405.

Casella, D., G. Panegrossi, P. Sanò, A. C. Marra, S. Dietrich, B. T. Johnson, and M. S. Kulie, 2017: Evaluation of the GPM-DPR snowfall detection capability: Comparison with CloudSat-CPR. *Atmos. Res.*, **197**, 64–75, https://doi.org/10.1016/j.atmosres.2017.06.018.

Delanoë, J., and R. Hogan, 2008: A variational scheme for retrieving ice cloud properties from combined radar, lidar, and infrared radiometer. *J. Geophys. Res.*, **113**, D07204, https://doi.org/10.1029/2007JD009000.

Derin, Y., and Coauthors, 2016: Multiregional satellite precipitation products evaluation over complex terrain. *J. Hydrometeor.*, **17**, 1817–1836, https://doi.org/10.1175/JHM-D-15-0197.1.

Durden, S. L., Z. S. Haddad, A. Kitiyakara, and F. K. Li, 1998: Effects of nonuniform beam filling on rainfall retrieval for the TRMM Precipitation Radar. *J. Atmos. Oceanic Tech.*, **15**, 635–646, https://doi.org/10.1175/1520-0426(1998)015<0635:EONBFO>2.0.CO;2.

Ebtehaj, A. M., and C. D. Kummerow, 2017: Microwave retrievals of terrestrial precipitation over snow-covered surfaces: A lesson from the GPM satellite. *Geophys. Res. Lett.*, **44**, 6154–6162, https://doi.org/10.1002/2017GL073451.

Fassnacht, S. R., 2004: Estimating Alter-shielded gauge snowfall undercatch, snowpack sublimation, and blowing snow transport at six sites in the coterminous USA. *Hydrol. Processes*, **18**, 3481–3492, https://doi.org/10.1002/hyp.5806.

Ferraro, R. R., and Coauthors, 2005: NOAA operational hydrological products derived from the Advanced Microwave Sounding Unit. *IEEE Trans. Geosci. Remote Sens.*, **43**, 1036–1049, https://doi.org/10.1109/TGRS.2004.843249.

Grecu, M., and W. S. Olson, 2020: Precipitation retrievals from satellite combined radar and radiometer observations, *Satellite Precipitation Measurement*, Advances in Global Change Research, Vol. 1, Springer, 231–248, https://doi.org/10.1007/978-3-030-24568-9_13.

——, ——, and E. N. Anagnostou, 2004: Retrieval of precipitation profiles from multiresolution, multifrequency active and passive microwave observations. *J. Appl. Meteor.*, **43**, 562–575, https://doi.org/10.1175/1520-0450(2004)043<0562:ROPPFM>2.0.CO;2.

——, ——, S. J. Munchak, S. Ringerud, L. Liao, Z. Haddad, B. L. Kelley, and S. F. McLaughlin, 2016: The GPM combined algorithm. *J. Atmos. Oceanic Technol.*, **33**, 2225–2245, https://doi.org/10.1175/JTECH-D-16-0019.1.

Heidke, P., 1926: Berechnung des Erfolges und der Güte der Windstärkevorhersagen im Sturmwarnungsdienst. *Geogr. Ann.*, **8**, 301–349.

Hitschfeld, W., and J. Bordan, 1954: Errors inherent in the radar measurement of rainfall at attenuating wavelengths. *J. Meteor.*, **11**, 58–67, https://doi.org/10.1175/1520-0469(1954)011<0058:EIITRM>2.0.CO;2.

Hogan, R. J., and A. Battaglia, 2008: Fast lidar and radar multiple-scattering models. Part II: Wide-angle scattering using the time-dependent two-stream approximation. *J. Atmos. Sci.*, **65**, 3636–3651, https://doi.org/10.1175/2008JAS2643.1.

Iguchi, T., and R. Meneghini, 2016a: GPM DPR Ka precipitation profile 2A 1.5 hours 5 km V06. GES DISC, accessed 10 December 2020, https://doi.org/10.5067/GPM/DPR/Ka/2A/06.

——, and ——, 2016b: GPM DPR Ku precipitation profile 2A 1.5 hours 5 km V06. GES DISC, accessed 10 December, 2020, https://doi.org/10.5067/GPM/DPR/Ku/2A/06.

——, and ——, 2016c: GPM GMI (GPROF) radiometer precipitation profiling L2A 1.5 hours 13 km V05. GES DISC, accessed 10 December 2020, https://doi.org/10.5067/GPM/GMI/GPM/GPROF/2A/05.

——, and ——, 2017: GPM DPR precipitation profile L2A 1.5 hours 5 km V06. GES DISC, accessed 10 December 2020, https://doi.org/10.5067/GPM/DPR/GPM/2A/06.

——, T. Kozu, R. Meneghini, J. Awaka, and K. Okamoto, 2000: Rain-profiling algorithm for the TRMM Precipitation Radar. *J. Appl. Meteor.*, **39**, 2038–2052, https://doi.org/10.1175/1520-0450(2001)040<2038:RPAFTT>2.0.CO;2.

IPCC, 2013: *Climate Change 2013: The Physical Science Basis.* Cambridge University Press, 1535 pp., https://doi.org/10.1017/CBO9781107415324.

Joe, P., and Coauthors, 2010: The Polar Precipitation Measurement mission. *Proc. Sixth European Conf. on Radar Meteorology and Hydrology*, Sibiu, Romania, ERAD.

Kidd, C., J. Tan, P.-E. Kirstetter, and W. A. Petersen, 2018: Validation of the version 05 level 2 precipitation products from the GPM Core Observatory and constellation satellite sensors. *Quart. J. Roy. Meteor. Soc.*, **144**, 313–328, https://doi.org/10.1002/qj.3175.

Kim, D., B. Nelson, and D.-J. Seo, 2009: Characteristics of reprocessed Hydrometeorological Automated Data System (HADS) hourly precipitation data. *Wea. Forecasting*, **24**, 1287–1296, https://doi.org/10.1175/2009WAF2222227.1.

Kirstetter, P.-E., and Coauthors, 2012: Toward a framework for systematic error modeling of spaceborne precipitation radar with NOAA/NSSL ground radar–based National Mosaic QPE. *J. Hydrometeor.*, **13**, 1285–1300, https://doi.org/10.1175/JHM-D-11-0139.1.

——, J. J. Gourley, Y. Hong, J. Zhang, S. Moazamigoodarzi, C. Langston, and A. Arthur, 2015: Probabilistic precipitation rate estimates with ground-based radar networks. *Water Resour. Res.*, **51**, 1422–1442, https://doi.org/10.1002/2014WR015672.

Kirstetter, P. E., W. A. Petersen, and J. J. Gourley, 2018: GPM Ground Validation Multi-Radar/Multi-Sensor (MRMS) precipitation reanalysis for satellite validation product. NASA Global Hydrology Resource Center DAAC, accessed 1 August 2020, https://doi.org/10.5067/GPMGV/MRMS/DATA101.

Kneifel, S., U. Löhnert, A. Battaglia, S. Crewell, and D. Siebler, 2010: Snow scattering signals in ground-based passive microwave radiometer measurements. *J. Geophys. Res.*, **115**, D16214, https://doi.org/10.1029/2010JD013856.

——, J. Leinonen, J. Tyynela, D. Ori, and A. Battaglia, 2020: Scattering of hydrometeors. *Satellite Precipitation Measurement*, Advances in Global Change Research, Vol. 1, Springer Nature, 249–276, https://doi.org/10.1007/978-3-030-24568-9_13.

Kollias, P., E. E. Clothiaux, M. A. Miller, B. A. Albrecht, G. L. Stephens, and T. P. Ackerman, 2007: Millimeter-wavelength radars: New frontier in atmospheric cloud and precipitation research. *Bull. Amer. Meteor. Soc.*, **88**, 1608–1624, https://doi.org/10.1175/BAMS-88-10-1608.

Kongoli, C., P. Pellegrino, R. R. Ferraro, N. C. Grody, and H. Meng, 2003: A new snowfall detection algorithm over land using measurements from the Advanced Microwave Sounding Unit (AMSU). *Geophys. Res. Lett.*, **30**, 1756, https://doi.org/10.1029/2003GL017177.

——, H. Meng, J. Dong, and R. Ferraro, 2015: A snowfall detection algorithm over land utilizing high-frequency passive microwave measurements—Application to ATMS. *J. Geophys. Res. Atmos.*, **120**, 1918–1932, https://doi.org/10.1002/2014JD022427.

Kulie, M. S., L. Milani, N. B. Wood, S. A. Tushaus, R. Bennartz, and T. S. L'Ecuyer, 2016: A shallow cumuliform snowfall census using spaceborne radar. *J. Hydrometeor.*, **17**, 1261–1279, https://doi.org/10.1175/JHM-D-15-0123.1.

——, ——, ——, and T. S. L'Ecuyer, 2020: Global snowfall detection and measurement. *Satellite Precipitation Measurement*, Advances in Global Change Research, Vol. 2, Springer Nature, 277–296, https://doi.org/10.1007/978-3-030-35798-6_12.

Kummerow, C. D., D. L. Randel, M. Kulie, N.-Y. Wang, R. Ferraro, S. Joseph Munchak, and V. Petkovic, 2015: The evolution of the Goddard profiling algorithm to a fully parametric scheme. *J. Atmos. Oceanic Technol.*, **32**, 2265–2280, https://doi.org/10.1175/JTECH-D-15-0039.1.

Kuo, K.-S., and Coauthors, 2016: The microwave radiative properties of falling snow derived from nonspherical ice particle

models. Part I: An extensive database of simulated pristine crystals and aggregate particles, and their scattering properties. *J. Appl. Meteor. Climatol.*, **55**, 691–708, https://doi.org/10.1175/JAMC-D-15-0130.1.

Lau, W. K.-M., H.-T. Wu, and K.-M. Kim, 2013: A canonical response of precipitation characteristics to global warming from CMIP5 models. *Geophys. Res. Lett.*, **40**, 3163–3169, https://doi.org/10.1002/grl.50420.

Le, M., and V. Chandrasekar, 2019: Ground validation of surface snowfall algorithm in GPM Dual-Frequency Precipitation Radar. *J. Atmos. Oceanic Tech.*, **36**, 607–619, https://doi.org/10.1175/JTECH-D-18-0098.1.

L'Ecuyer, T. S., and Coauthors, 2015: The observed state of the energy budget in the early twenty-first century. *J. Climate*, **28**, 8319–8346, https://doi.org/10.1175/JCLI-D-14-00556.1.

Lettenmaier, D. P., D. Alsdorf, J. Dozier, G. J. Huffman, M. Pan, and E. F. Wood, 2015: Inroads of remote sensing into hydrologic science during the WRR era. *Water Resour. Res.*, **51**, 7309–7342, https://doi.org/10.1002/2015WR017616.

Levizzani, V., S. Laviola, and E. Cattani, 2011: Detection and measurement of snowfall from space. *Remote Sens.*, **3**, 145–166, https://doi.org/10.3390/rs3010145.

Liao, L., and R. Meneghini, 2019: Physical evaluation of GPM DPR single- and dual-wavelength algorithms. *J. Atmos. Oceanic Tech.*, **36**, 883–902, https://doi.org/10.1175/JTECH-D-18-0210.1.

Liu, G., 2020: Radar snowfall measurements. *Satellite Precipitation Measurement*, Advances in Global Change Research, Vol. 1, Springer Nature, 277–296, https://doi.org/10.1007/978-3-030-24568-9_13.

——, and J. A. Curry, 1997: Precipitation characteristics in Greenland-Iceland-Norwegian Seas determined by using satellite microwave data. *J. Geophys. Res.*, **102**, 13 987–13 997, https://doi.org/10.1029/96JD03090.

——, and E.-K. Seo, 2013: Detecting snowfall over land by satellite high-frequency microwave observations: The lack of scattering signature and a statistical approach. *J. Geophys. Res. Atmos.*, **118**, 1376–1387, https://doi.org/10.1002/jgrd.50172.

Marshall, J. S., and W. M. K. Palmer, 1948: The distribution of raindrops with size. *J. Atmos. Sci.*, **5**, 165–166, https://doi.org/10.1175/1520-0469(1948)005<0165:TDORWS>2.0.CO;2.

Martinaitis, S. M., S. B. Cocks, Y. Qi, B. T. Kaney, J. Zhang, and K. Howard, 2015: Understanding winter precipitation impacts on automated gauge observations within a real-time system. *J. Hydrometeor.*, **16**, 2345–2363, https://doi.org/10.1175/JHM-D-15-0020.1.

Matrosov, S. Y., 2019: Comparative evaluation of snowfall retrievals from the CloudSat W-band radar using ground-based weather radars. *J. Atmos. Oceanic Technol.*, **36**, 101–111, https://doi.org/10.1175/JTECH-D-18-0069.1.

——, and A. Battaglia, 2009: Influence of multiple scattering on CloudSat measurements in snow: A model study. *Geophys. Res. Lett.*, **36**, L12806, https://doi.org/10.1029/2009GL038704.

Meneghini, R., T. Iguchi, T. Kozu, L. Liao, K. Okamoto, J. A. Jones, and J. Kwiatkowski, 2000: Use of the surface reference technique for path attenuation estimates from the TRMM Precipitation Radar. *J. Appl. Meteor.*, **39**, 2053–2070, https://doi.org/10.1175/1520-0450(2001)040<2053:UOTSRT>2.0.CO;2.

Meng, H., C. Kongoli, and R. R. Ferraro, 2020: A 1DVAR-based snowfall rate algorithm for passive microwave radiometers. *Satellite Precipitation Measurement*, Advances in Global Change Research, Vol. 1, Springer Nature, 297–314, https://doi.org/10.1007/978-3-030-24568-9_13.

Milani, L., and Coauthors, 2018: CloudSat snowfall estimates over Antarctica and the Southern Ocean: An assessment of independent retrieval methodologies and multi-year snowfall analysis. *Atmos. Res.*, **213**, 121–135, https://doi.org/10.1016/j.atmosres.2018.05.015.

Miller, P. A., M. F. Barth, L. A. Benjamin, R. S. Artz, and W. R. Pendergrass, 2007: MADIS support for UrbaNet. *14th Symp. on Meteorological Observation and Instrumentation/16th Conf. on Applied Climatology*, San Antonio, TX, Amer. Meteor. Soc., JP2.5, http://ams.confex.com/ams/pdfpapers/119116.pdf.

Mitchell, D. L., 1996: Use of mass- and area-dimensional power laws for determining precipitation particle terminal velocities. *J. Atmos. Sci.*, **53**, 1710–1723, https://doi.org/10.1175/1520-0469(1996)053<1710:UOMAAD>2.0.CO;2.

Mroz, K., A. Battaglia, T. J. Lang, D. J. Cecil, S. Tanelli, and F. Tridon, 2017: Hail-detection algorithm for the GPM *Core Observatory* satellite sensors. *J. Appl. Meteor. Climatol.*, **56**, 1939–1957, https://doi.org/10.1175/JAMC-D-16-0368.1.

Munchak, S. J., S. Ringerud, L. Brucker, Y. You, I. de Gelis, and C. Prigent, 2020: An active-passive microwave land surface database from GPM. *IEEE Trans. Geosci. Remote Sens.*, **58**, 6224–6242, https://doi.org/10.1109/TGRS.2020.2975477.

Navarro, A., E. Garcia-Ortega, A. Merino, J. L. Sanchez, C. Kummerow, and F. J. Tapiador, 2019: Assessment of IMERG precipitation estimates over Europe. *Remote Sens.*, **11**, 2470, https://doi.org/10.3390/rs11212470.

Noh, Y.-J., G. Liu, A. S. Jones, and T. H. Vonder Haar, 2009: Toward snowfall retrieval over land by combining satellite and in situ measurements. *J. Geophys. Res.*, **114**, D24205, https://doi.org/10.1029/2009JD012307.

Norin, L., A. Devasthale, T. S. L'Ecuyer, N. B. Wood, and M. Smalley, 2015: Intercomparison of snowfall estimates derived from the CloudSat Cloud Profiling Radar and the ground-based weather radar network over Sweden. *Atmos. Meas. Tech.*, **8**, 5009–5021, https://doi.org/10.5194/amt-8-5009-2015.

Olson, W., 2017: GPM DPR and GMI combined precipitation L2B 1.5 hours 5 km V06. GES DISC, accessed 10 December, 2020, https://doi.org/10.5067/GPM/DPRGMI/CMB/2B/06.

Palerme, C., J. E. Kay, C. Genthon, T. L'Ecuyer, N. B. Wood, and C. Claud, 2014: How much snow falls on the Antarctic ice sheet? *Cryosphere*, **8**, 1577–1587, https://doi.org/10.5194/tc-8-1577-2014.

——, C. Claud, N. B. Wood, T. L'Ecuyer, and C. Genthon, 2019: How does ground clutter affect CloudSat snowfall retrievals over ice sheets? *IEEE Geosci. Remote Sens. Lett.*, **16**, 342–346, https://doi.org/10.1109/LGRS.2018.2875007.

Panegrossi, G., J.-F. Rysman, D. Casella, A. C. Marra, P. Sanò, and M. S. Kulie, 2017: CloudSat-based assessment of GPM Microwave Imager snowfall observation capabilities. *Remote Sens.*, **9**, 1263, https://doi.org/10.3390/rs9121263.

Petty, G. W., and W. Huang, 2010: Microwave backscatter and extinction by soft ice spheres and complex snow aggregates. *J. Atmos. Sci.*, **67**, 769–787, https://doi.org/10.1175/2009JAS3146.1.

Rasmussen, R., and Coauthors, 2012: How well are we measuring snow: The NOAA/FAA/NCAR winter precipitation test bed. *Bull. Amer. Meteor. Soc.*, **93**, 811–829, https://doi.org/10.1175/BAMS-D-11-00052.1.

Rodgers, C. D., 2000: *Inverse Methods for Atmospheric Sounding*. World Scientific, 238 pp., https://doi.org/10.1142/3171.

Romanov, P., G. Gutman, and I. Csiszar, 2000: Automated monitoring of snow cover over North America with multispectral satellite data. *J. Appl. Meteor.*, **39**, 1866–1880, https://doi.org/10.1175/1520-0450(2000)039<1866:AMOSCO>2.0.CO;2.

Rysman, J.-F., G. Panegrossi, P. Sanò, A. Marra, S. Dietrich, L. Milani, and M. Kulie, 2018: SLALOM: An all-surface snow water path retrieval algorithm for the GPM Microwave Imager. *Remote Sens.*, **10**, 1278, https://doi.org/10.3390/rs10081278.

——, and Coauthors, 2019: Retrieving surface snowfall with the GPM Microwave Imager: A new module for the SLALOM algorithm. *Geophys. Res. Lett.*, **46**, 13 593–13 601, https://doi.org/10.1029/2019GL084576.

Seto, S., and T. Iguchi, 2015: Intercomparison of attenuation correction methods for the GPM Dual-Frequency Precipitation Radar. *J. Atmos. Oceanic Tech.*, **32**, 915–926, https://doi.org/10.1175/JTECH-D-14-00065.1.

——, and T. Kinoshita, 2015: Relation between precipitation rate and mass weighted mean diameter and its validation for the DPR algorithms. *Annual Conf.*, Tokyo, Japan, Hydrology and Water Resources Society, 100063, https://doi.org/10.11520/jshwr.28.0_100063.

——, and T. Shimozuma, 2015: Relations between precipitation rate and mass weighted mean diameter for the GPM/DPR algorithm. *2015 Fall Meeting*, San Francisco, CA, Amer. Geophys. Union, Abstract H12E-03.

Sims, E. M., and G. Liu, 2015: A parameterization of the probability of snow–rain transition. *J. Hydrometeor.*, **16**, 1466–1477, https://doi.org/10.1175/JHM-D-14-0211.1.

Skofronick-Jackson, G., and B. T. Johnson, 2011: Surface and atmospheric contributions to passive microwave brightness temperatures for falling snow events. *J. Geophys. Res.*, **116**, D02213, https://doi.org/10.1029/2010JD014438.

——, and Coauthors, 2017: The Global Precipitation Measurement (GPM) mission for science and society. *Bulletin of the Amer. Meteor. Soc.*, **98**, 1679–1695, https://doi.org/10.1175/BAMS-D-15-00306.1.

——, M. Kulie, L. Milani, S. J. Munchak, N. B. Wood, and V. Levizzani, 2019: Satellite estimation of falling snow: A Global Precipitation Measurement (GPM) *Core Observatory* perspective. *J. Appl. Meteor. Climatol.*, **58**, 1429–1448, https://doi.org/10.1175/JAMC-D-18-0124.1.

Smalley, M., P.-E. Kirstetter, and T. L'Ecuyer, 2017: How frequent is precipitation over the contiguous United States? Perspectives from ground-based and spaceborne radars. *J. Hydrometeor.*, **18**, 1657–1672, https://doi.org/10.1175/JHM-D-16-0242.1.

Stephens, G. L., and Coauthors, 2012: An update on Earth's energy balance in light of the latest global observations. *Nat. Geosci.*, **5**, 691–696, https://doi.org/10.1038/ngeo1580.

——, D. Winker, J. Pelon, C. Trepte, D. Vane, C. Yuhas, T. L'Écuyer, and M. Lebsock, 2018: *CloudSat* and *CALIPSO* within the A-train: Ten years of actively observing the Earth system. *Bull. Amer. Meteor. Soc.*, **99**, 569–581, https://doi.org/10.1175/BAMS-D-16-0324.1.

Surussavadee, C., and D. H. Staelin, 2009: Satellite retrievals of Arctic and equatorial rain and snowfall rates using millimeter wavelengths. *IEEE Trans. Geosci. Remote Sens.*, **47**, 3697–3707, https://doi.org/10.1109/TGRS.2009.2029093.

Takbiri, Z., A. Ebtehaj, E. Foufoula-Georgiou, P.-E. Kirstetter, and F. J. Turk, 2019: A prognostic nested *k*-nearest approach for microwave precipitation phase detection over snow cover. *J. Hydrometeor.*, **20**, 251–274, https://doi.org/10.1175/JHM-D-18-0021.1.

Tanelli, S., S. L. Durden, E. Im, K. S. Pak, D. G. Reinke, P. Partain, J. M. Haynes, and R. T. Marchand, 2008: CloudSat's cloud profiling radar after two years in orbit: Performance, calibration, and processing. *IEEE Trans. Geosci. Remote Sens.*, **46**, 3560–3573, https://doi.org/10.1109/TGRS.2008.2002030.

Testud, J., S. Oury, R. A. Black, P. Amayenc, and X. Dou, 2001: The concept of "normalized" distribution to describe raindrop spectra: A tool for cloud physics and cloud remote sensing. *J. Appl. Meteor.*, **40**, 1118–1140, https://doi.org/10.1175/1520-0450(2001)040<1118:TCONDT>2.0.CO;2.

Turk, F. J., 2016: CloudSat-GPM coincidence dataset: Version 1C. JPL Rep., 18 pp., https://gpm.nasa.gov/sites/default/files/document_files/CSATGPM_COIN_ATBD.pdf.

——, Z. S. Haddad, and Y. You, 2014: Principal components of multifrequency microwave land surface emissivities. Part I: Estimation under clear and precipitating conditions. *J. Hydrometeor.*, **15**, 3–19, https://doi.org/10.1175/JHM-D-13-08.1.

von Lerber, A., D. Moisseev, D. A. Marks, W. Petersen, A.-M. Harri, and V. Chandrasekar, 2018: Validation of GMI snowfall observations by using a combination of weather radar and surface measurements. *J. Appl. Meteor. Climatol.*, **57**, 797–820, https://doi.org/10.1175/JAMC-D-17-0176.1.

Wang, Y., G. Liu, E.-K. Seo, and Y. Fu, 2013: Liquid water in snowing clouds: Implications for satellite remote sensing of snowfall. *Atmos. Res.*, **131**, 60–72, https://doi.org/10.1016/j.atmosres.2012.06.008.

Watters, D., A. Battaglia, K. Mroz, and F. Tridon, 2018: Validation of the GPM version-5 surface rainfall products over Great Britain and Ireland. *J. Hydrol.*, **19**, 1617–1636, https://doi.org/10.1175/JHM-D-18-0051.1.

Wen, Y., P. Kirstetter, J. J. Gourley, Y. Hong, A. Behrangi, and Z. Flamig, 2017: Evaluation of MRMS snowfall products over the western United States. *J. Hydrometeor.*, **18**, 1707–1713, https://doi.org/10.1175/JHM-D-16-0266.1.

Wood, N. B., and T. S. L'Ecuyer, 2018: Level 2C snow profile process description and interface control document: Product version P1 R05. NASA Doc., 26 pp.

You, Y., N.-Y. Wang, and R. Ferraro, 2015: A prototype precipitation retrieval algorithm over land using passive microwave observations stratified by surface condition and precipitation vertical structure. *J. Geophys. Res. Atmos.*, **120**, 5295–5315, https://doi.org/10.1002/2014JD022534.

——, ——, ——, and P. Meyers, 2016: A prototype precipitation retrieval algorithm over land for ATMS. *J. Hydrometeor.*, **17**, 1601–1621, https://doi.org/10.1175/JHM-D-15-0163.1.

Zhang, J., and J. Gourley, 2018: Multi-Radar Multi-Sensor Precipitation Reanalysis (version 1.0). Open Commons Consortium Environmental Data Commons, accessed 31 March 2020, https://doi.org/10.25638/EDC.PRECIP.0001.

——, and Coauthors, 2016: Multi-Radar Multi-Sensor (MRMS) quantitative precipitation estimation: Initial operating capabilities. *Bull. Amer. Meteor. Soc.*, **97**, 621–638, https://doi.org/10.1175/BAMS-D-14-00174.1.

Zhang, L., D. Lu, S. Duan, and J. Liu, 2004: Small-scale rain nonuniformity and its effect on evaluation of nonuniform beam-filling error for spaceborne radar rain measurement. *J. Atmos. Oceanic Tech.*, **21**, 1190–1197, https://doi.org/10.1175/1520-0426(2004)021<1190:SRNAIE>2.0.CO;2.